Received: 12 January 2021 | Revised: 7 July 2021 | Accepted: 14 July 2021 | Published on: 16 August 2021

DOI: 10.1002/qj.4133

Quarterly Journal of the Royal Meteorological Society

RESEARCH ARTICLE

Tropical cyclone life cycle in a three-dimensional numerical simulation

Roger K. Smith[1] | **Gerard Kilroy**[1] | **M. T. Montgomery**[2]

[1]Meteorological Institute, Ludwig Maximilians University of Munich, Munich, Germany

[2]Department of Meteorology, Naval Postgraduate School, Monterey, California

Correspondence
R.K. Smith, Meteorological Institute, Ludwig-Maximilians University of Munich, Theresienstrasse 37, 80333 Munich, Germany.
Email: roger.smith@lmu.de

Funding information
U.S. Office of Naval Research, Grant/Award Numbers: N0001417WX00336, N0001420WX01473; German Research Council, Grant/Award Number: KI-2248

Abstract

An idealized, three-dimensional, numerical simulation of tropical cyclone evolution in a quiescent environment on an f-plane is used to explore aspects of the cyclone's life cycle in the context of the rotating-convection paradigm. In the 20-day simulation, the vortex undergoes a life cycle including a gestation period culminating in genesis, a rapid intensification phase, a mature phase, a transient decay and re-intensification phase, a second mature phase and a rapid decay phase. During much of the life cycle, the flow evolution is highly asymmetric, although important aspects of it can be understood within an azimuthally averaged framework, central to which are a boundary-layer control mechanism and a new ventilation diagnostic. The boundary-layer control mechanism provides an explanation for the gradual expansion of the inner core of the vortex. The ventilation diagnostic characterizes the ability of deep convection within a given radius to evacuate the mass of air ascending out of the boundary layer within that radius. The transient decay and re-intensification phase is not associated with an eyewall replacement cycle, but rather with a hitherto undescribed process in which the eyewall becomes fragmented as a rainband complex forms beyond it. This process is interpreted as an interplay between the boundary layer and ventilation. The final rapid decay of the vortex results from the ever increasing difficulty of deep convection to ventilate the air exiting the boundary layer. Any unventilated air flows radially outwards in the lower troposphere and leads to spin-down because of the approximate conservation of mean absolute angular momentum. If found in real cyclones, such transience or final decay might be erroneously attributed to ambient vertical wind shear. The results support the hypothesis that, even in a quiescent environment, isolated tropical cyclone vortices are intrinsically transient and never reach a globally steady state.

KEYWORDS

boundary layer, hurricane, tropical cyclone, typhoon, ventilation, vortex decay, vortex intensification

---

1 | INTRODUCTION

The last decade has seen the development of a unified conceptual model for understanding tropical cyclone genesis and intensification in three dimensions, the so-called rotating convection paradigm (Montgomery and Smith, 2014; Smith and Montgomery, 2016; Montgomery and Smith, 2017b). Its development so far has been mainly within the context of the prototype problem for intensification that considers the evolution of a weak, initially cloud-free, warm-cored, axisymmetric vortex in gradient wind and hydrostatic balance in a quiescent environment on an f-plane.

At a basic level, the conceptual model considers a cluster of deep convective clouds that persist in a region of sufficient ambient cyclonic rotation over a warm tropical ocean. Collectively, these deep clouds generate a cluster-scale overturning circulation. The inward branch of this circulation converges absolute vorticity in the lower troposphere, which by Stokes' theorem leads to an amplification of the mean tangential velocity at a given radius from the centre of the cluster. In the divergent branch of the circulation in the upper troposphere, absolute vorticity is advected away from the centre leading to a spin-down of the tangential velocity component and even to a sign reversal beyond a certain radius.

The persistence of deep convection requires a sufficiently rapid moisture supply from the ocean to maintain convective instability and is favoured by a progressive local moistening of the troposphere within the cluster through the evaporation of previous clouds (e.g., Nolan, 2007; figure 8c of Kilroy *et al.*, 2017b). The moistening serves to support robust updraughts (Kilroy and Smith, 2012) and to reduce the strength of convective downdraughts, which would otherwise lead to convective stabilization (Emanuel, 1986). The local amplification of vorticity by deep convection is a prominent feature of vortex evolution and the stochastic nature of the convection introduces a stochastic element to the evolution of the vorticity field (section 5 of Kilroy *et al.*, 2017b).

From an azimuthally averaged perspective, the paradigm includes, but extends, the classical axisymmetric paradigm for vortex intensification[1] articulated by Ooyama (1969) to explain the observed occurrence of the maximum tangential winds in the boundary layer (e.g., Kepert, 2006a; Kepert, 2006b; Bell and Montgomery, 2008; Montgomery *et al.*, 2014; Sanger *et al.*, 2014). Furthermore, it provides an overarching framework for understanding the complex convective and vortical processes in simulated and observed tropical cyclones, taking into account both azimuthal mean and eddy contributions to the dynamics and thermodynamics of vortex spin-up (Reasor *et al.*, 2009; Persing *et al.*, 2013; Guimond *et al.*, 2016a; Smith *et al.*, 2016; Montgomery *et al.*, 2020).

As far as we are aware, the long-term behaviour of tropical cyclones has received comparatively little attention. In particular, it has been common in some previous theoretical and numerical studies to assume that storms eventually reach a steady or quasi-steady state (Emanuel, 1986, henceforth E86; Emanuel, 1988; Emanuel, 1995; Bister and Emanuel, 1998 and later generalizations by Wirth and Dunkerton, 2006; Bryan and Rotunno, 2009; Hakim, 2011). However, Smith *et al.* (2014) and Persing *et al.* (2019) showed that, without a sustained source of cyclonic relative angular momentum, a vortex must ultimately decay, confirming earlier suggestions by Anthes (1974) p. 511, and Ooyama (1982) section 2. In particular, they noted that, while the definition of the quasi-steady mature phase in numerical simulations is commonly based on a later time period in which the maximum tangential velocity becomes approximately steady, the broader-scale vortex structure is by no means quasi-steady during this period. Typically, the storm continues to expand in outer size and the upper anticyclone continues to evolve.

Motivated by this finding, Kilroy *et al.* (2016) examined the long-term behaviour of a simulated tropical cyclone using the Pennsylvania State University/National Center for Atmospheric Research mesoscale model (MM5). They showed that, after reaching a mature intensity, the model storm progressively decays, although both the inner-core size, characterized by the radius of the eyewall, and the size of the outer circulation (measured, for example, by the radius of the gale-force winds) progressively increase for a period of time before the collapse of the vortex. This subsequent evolution of the mature vortex was explained in terms of a boundary-layer control mechanism in which the expansion of the azimuthally averaged tangential velocity component in the lower troposphere leads, through boundary-layer dynamics, to an increase in the radii of forced eyewall ascent as well as to a reduction in the maximum tangential wind speed in the boundary layer. These changes are accompanied by changes in the radial and vertical distribution of diabatic heating, in part because the surface enthalpy flux changes in response to the changing surface wind and, in part, because of the changing radial distribution of vertical velocity of air exiting the boundary layer. Kilroy *et al.*, pointed out that, as long

---

[1] In the classical paradigm, inflow in the lower troposphere induced by deep convection within the vortex circulation is argued to draw absolute angular momentum surfaces inwards. Above the frictional boundary layer, absolute angular momentum, M, is approximately materially conserved so that the inward movement of these surfaces implies a local spin-up of the tangential velocity component.

as the aggregate effect of inner-core deep convection is able to draw surfaces of absolute angular momentum, M, inwards, the outer circulation will continue to expand in size.

Of course, the foregoing discussion and analyses presume that subgrid-scale processes do not have a dominant effect on the vortex evolution at long times. The impact of explicit and/or implicit diffusion is model-dependent. An extended study of this issue for hurricane models has been conducted by Guimond *et al.* (2016a).

Within the framework of the rotating-convection paradigm applied to the prototype problem described earlier, this study aims to further investigate the life cycle of vortex evolution with a primary focus on the mature and decay phases. After showing a variety of metrics characterizing the vortex evolution (Section 3), we go on in Section 4 to examine horizontal cross-sections of low-level wind and vorticity structure in the inner-core region, highlighting in particular the markedly asymmetric nature of the decay phase. In Sections 5 and 6, we focus mainly on azimuthally averaged aspects of the simulation, which include the asymmetric eddy and wave effects associated with local deep convection, vortex Rossby waves and inertia-buoyancy waves.

New insights into the vortex evolution are presented in Section 6, where it is shown that much of the evolution, especially in the mature and decay phases, can be interpreted in terms of a boundary-layer control mechanism. To this end, we carry out a novel analysis of the ability of deep convection to ventilate the air that is converging in the boundary layer during various phases of the storm's life cycle and we introduce there a ventilation diagnostic (Section 6.4). A more in-depth investigation of the flow asymmetries that form during the decay phase will be part of a future study. The conclusions are presented in Section 7.

2 | THE NUMERICAL MODEL CONFIGURATION

The simulation to be described uses version 19 of the three-dimensional, non-hydrostatic cloud model CM1 (Bryan and Fritch 2002). The model has prediction equations for the three components of the velocity vector, specific humidity, suspended liquid, perturbation Exner function, and perturbation density potential temperature, where perturbation quantities are defined relative to a prescribed hydrostatic basic state. For simplicity, cloud processes are represented by the Kessler warm rain scheme in which rain has a fixed fall speed of $7\,\mathrm{m{\cdot}s^{-1}}$. Ice microphysical processes and dissipative heating are not included.

The model configuration is similar to that described in section 2 of Črnivec *et al.* (2015), except that the time-scale for Newtonian relaxation to the temperature field is taken to be 10 days instead of the previous default CM1 value (12 hr). The reasons for this choice are discussed in the Appendix.

The model domain is 3,010 × 3,010 km, with 1,040 grid points in the zonal and meridional directions. The inner 600 × 600 km has a constant horizontal grid spacing of 1 km. Outside the inner 600 × 600 km, the grid spacing gradually stretches from 1 to 10 km. There are 40 vertical levels starting at a height of 25 m and extending upwards to a height of 25 km. There is variable grid spacing also in the vertical, smoothly changing from 50 m near the surface to 1,200 m near the model top. There are eight levels below 1.1 km height to provide an adequate resolution of the frictional boundary layer.

To suppress the artificial reflection of internal gravity waves from the upper boundary, a Rayleigh damping layer is added at heights above 20 km. The lateral boundaries are open radiative.

The background thermodynamic state is based on the Dunion moist tropical sounding (Dunion, 2011), which has a Convective Available Potential Energy (CAPE) of $2{,}104\,\mathrm{J{\cdot}kg^{-1}}$ and a Total Precipitable Water of $51.5\,\mathrm{kg{\cdot}m^{-2}}$. A latitude of 20°N and a constant sea surface temperature of 27 °C are chosen.

The subgrid-scale turbulence is represented by choosing option "iturb=3" in the model, which is designed for problems that do not resolve any part of the turbulent Kolmogorov inertial range. This choice requires the specification of the horizontal mixing length $l_\mathrm{h} = 700$ m and the vertical mixing length $l_\mathrm{v} = 50$ m. These values are based on the recent observational findings of Zhang and Montgomery (2012) and Zhang *et al.* (2011), respectively. They are close also to the values recommended by Bryan (2012) in order to produce realistic hurricane structure. For simplicity, these mixing lengths are assumed constant in both space and time.

The initial vortex is axisymmetric and in thermal wind balance. The initial tangential wind speed has a maximum value of $5\,\mathrm{m{\cdot}s^{-1}}$ at the surface and at a radius of 200 km. The tangential wind speed decreases sinusoidally with height, becoming zero at a height of 20 km. Above this height, the tangential wind is set to zero. The balanced pressure, density and temperature fields consistent with this prescribed tangential wind distribution are obtained using the method described by Smith (2006). Since the interest is in the long-term behaviour of the vortex, the calculations are carried out for 24 days with data output every 15 min. However, the vortex core moves out of the fine mesh domain just after 20 days, making detailed analyses after that time of limited value.

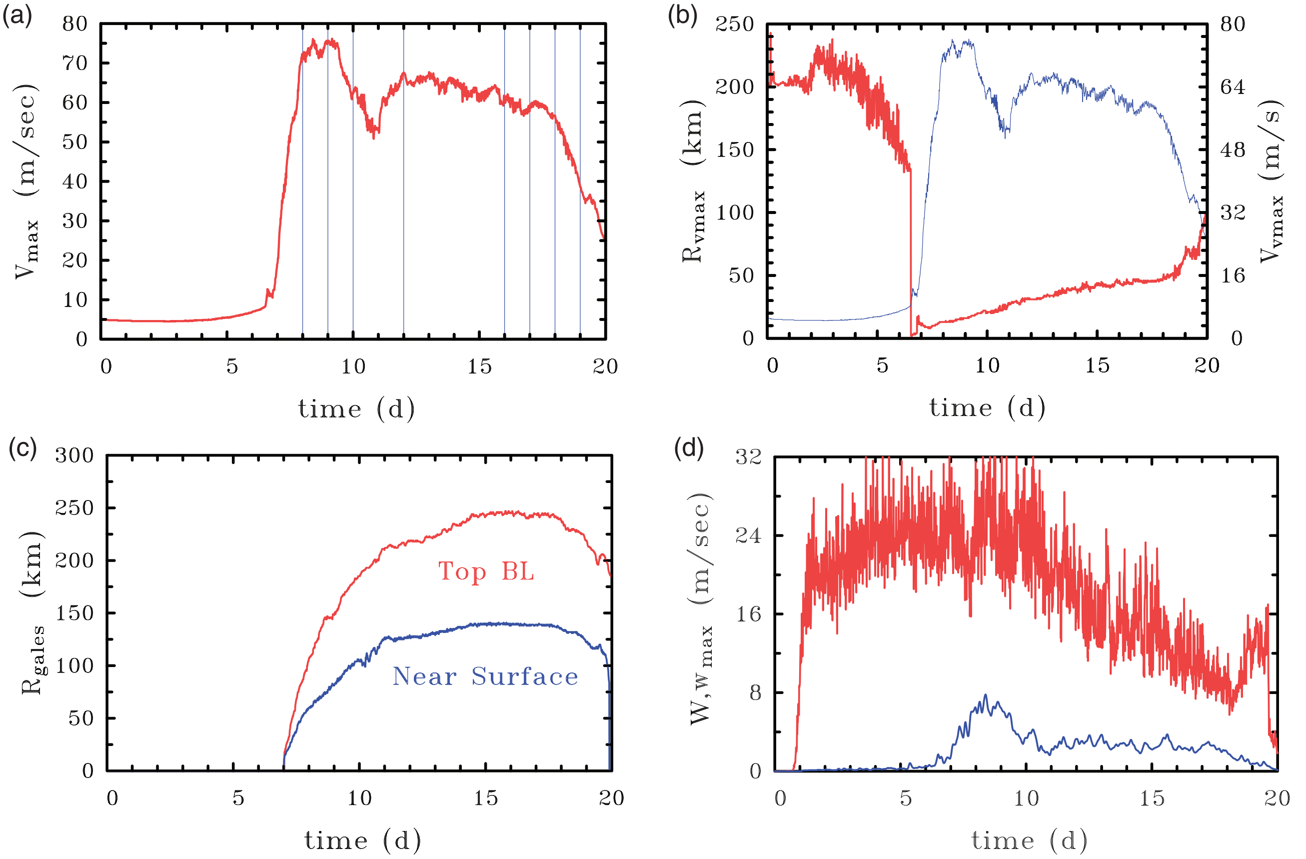

FIGURE 1 Time series of (a) maximum azimuthally averaged tangential wind speed ($V_{\max}$), (b) the radius $R_{V\max}$ at which $V_{\max}$ occurs, (c) the outermost radius of gale force (17 m·s^{-1}) azimuthally averaged tangential winds (R_{gales}), at a height of 1 km and the outermost radius R_{galesF} where the corresponding azimuthally averaged-surface wind speed falls below gale force, and (d) the maximum azimuthally averaged vertical velocity ($W_{\max}$; blue) and maximum local vertical velocity ($w_{\max}$; red). The thin vertical lines in (a) show times at which horizontal or vertical cross-sections are shown later in the text [Colour figure can be viewed at wileyonlinelibrary.com]

3 | VORTEX INTENSIFICATION, MATURITY AND DECAY

The focus of the present article is on the long-term (20-day) vortex behaviour in a single simulation. To set the scene, Figure 1 shows selected azimuthally averaged metrics which characterize the vortex evolution in this simulation. These metrics include the maximum tangential wind speed ($V_{\max}$), the radius at which this maximum occurs ($R_{V\max}$), two measures of vortex size, and the maximum vertical velocity, $W_{\max}$. Also shown is the maximum local vertical velocity, $w_{\max}$.

Following the definitions of Kilroy *et al.* (2017b), the outer core size is characterized by the outermost radius of gale force winds, R_{gales}, defined here as the radius of 17 m·s^{-1} azimuthally averaged tangential wind speed at a height of 1 km, which is approximately at the top of the boundary layer. The measure of size adopted by forecasters is defined as the (outer) radius at which total horizontal wind speed at a standard meteorological height of 10 m is 17 m·s^{-1}. In general, this radius will be a function of azimuth. Here we base the near-surface radius of gales, R_{galesF} on the azimuthally averaged total horizontal wind speed extrapolated from the lowest model level (25 m) to the surface.

After a gestation period lasting a little more than 6.5 days, the vortex undergoes a period of rapid intensification (RI; Figure 1a), which lasts about a day and a half. The maximum intensity is first reached at about 8.5 days with $V_{\max} = 75$ m·s^{-1}. The first mature phase, which could be considered as the period between 8 and 9.5 days, is relatively short-lived and is followed by a period of about a day and a half over which $V_{\max}$ declines to just over 50 m·s^{-1}. This decline is followed by a second period of RI in which $V_{\max}$ reaches about 65 m·s^{-1} at about 12 days.

It is worth noting that the intensity change between days 7 and 8 is 51 m·s^{-1}. This value exceeds the National Hurricane Center threshold for RI[2] by a factor of more than three, showing that, despite the simplifications made,

---

[2] The United States National Hurricane Center defines rapid intensification as an increase in the maximum sustained winds (based

the model is easily able to capture RI. It is worth noting also that the time variation of the maximum intensity simulated herein is not a result of environmental vertical shear, or lower sea surface temperatures, etc. Rather, the intensity and structure change represents an internal mode of variability that, in our view, must be understood as a prerequisite to understanding observed or simulated tropical cyclone intensity change in more complex situations.

After a second mature phase lasting about a day, $V_{\max}$ begins to decline, although with small amplitude fluctuations of intensity. The decay is relatively slow at first, with $V_{\max}$ falling to 57 m·s^{-1} by 18 days, but it becomes quite rapid thereafter with $V_{\max}$ falling well below hurricane strength (32 m·s^{-1}) by 20 days. As noted above, just after 20 days the vortex core wanders out of the inner uniform mesh domain and it is no longer possible to calculate the foregoing metrics with any accuracy. The height of $V_{\max}$ is typically below 1 km, within the frictional boundary layer (Section 5).

Shortly before the onset of RI, there is a sharp decline in R_{Vmax} (Figure 1b). This decline is related to the formation of a weak and very localized, but transient vortical circulation induced by a vigorous convective cell near the centre of the broadscale circulation. This vortical circulation has an R_{Vmax} of only 2 km with a $V_{\max}$ of 8.7 m·s^{-1}. At 6.5 days, R_{Vmax} jumps from 4 to 17 km and $V_{\max}$ jumps from 10.5 to 11.2 m·s^{-1} as a small vortex emerges from the convective cell. Thereafter, R_{Vmax} progressively increases. Both measures of size (R_{gales} and R_{galesF}) show a sharp increase as RI begins, but the rate of increase declines while remaining positive until about 17–18 days, after which both measures begin to decline.

The quantity $W_{\max}$ is one metric characterizing the strength of the azimuthally averaged overturning circulation. This quantity increases steadily during the period of RI and is largest during the first mature phase (Figure 1d). From about 9 days onwards, $W_{\max}$ declines steadily as the vortex decays. This behaviour would indicate that, up until the first mature phase, the near-surface moistening near the base of the eyewall outweighs the effect of upper-level warming that accompanies the vortex intensification so that convective instability (as measured by the CAPE) increases. However, beyond the first mature phase, the upper-level warming begins to dominate and convective instability progressively declines.

A complementary quantity to $W_{\max}$ is the maximum local updraught velocity $w_{\max}$. Figure 1d shows that, on the first day of the gestation period, which, itself lasts for approximately 6.5 days, $w_{\max}$ increases rapidly, reflecting the formation of the first deep convective clouds locally. Subsequently, $w_{\max}$ remains large until about 11 days, when its time mean, say over a few hours, progressively declines. This decline is another indication of decreasing convective instability associated with the upper-level warming. Not surprisingly, $w_{\max}$ is much larger than $W_{\max}$ since these deep convective clouds are highly asymmetric relative to a nominal circulation centre. Thus, during much of the vortex life cycle, the "deep convective eddies" are an important component of the mean transverse overturning circulation. The simulated maximum local updraught velocities are of similar order of magnitude to those estimated from airborne Doppler radar observations, typically 20–25 m·s^{-1} (Houze *et al.*, 2009; Guimond *et al.*, 2010).

4 | ASYMMETRIC VIEW OF VORTEX EVOLUTION

We begin by documenting the intrinsically asymmetric nature of the vortex evolution. Azimuthally averaged aspects are discussed in later sections. It turns out that the evolution during genesis and RI phases are quite similar to those described in Kilroy *et al.* (2017b) and in many observational studies (e.g., Houze *et al.*, 2009; Molinari and Vollaro, 2010; Rogers *et al.*, 2013; Guimond *et al.*, 2016b). In essence, areas of convectively generated low-level relative vorticity progressively organize into a monopole structure and isolated patches of deep convection organize towards an annular ring. In the modelling study of Kilroy *et al.*, considerable organization occurs even while maximum wind speeds remain light. For brevity we focus here on the mature and decay phases.

Figures 2 and 3 show horizontal cross-sections of the vertical component of relative vorticity and wind vectors at a height of 1 km at selected times of vortex evolution. They show also the 1 m·s^{-1} contours of vertical velocity at a height of 6 km, which indicate the location of strong, deep convective updraughts. Figure 2 shows selected times from 8 to 12 days, during the first mature phase and the subsequent period of intensity decline and recovery. Figure 3 shows similar daily fields from 16 to 19 days during the decay phase.

4.1 | Mature phase

Figure 2a shows the situation at 8 days, at the end of the RI phase and the start of the first mature phase when $V_{\max}$ now exceeds 70 m·s^{-1}. By this time, deep convection has formed in a closed "eyewall" around a large and

---

on a 1 min average) of a tropical cyclone of at least 30 knots (15 m·s^{-1}) in a 24 hr period.

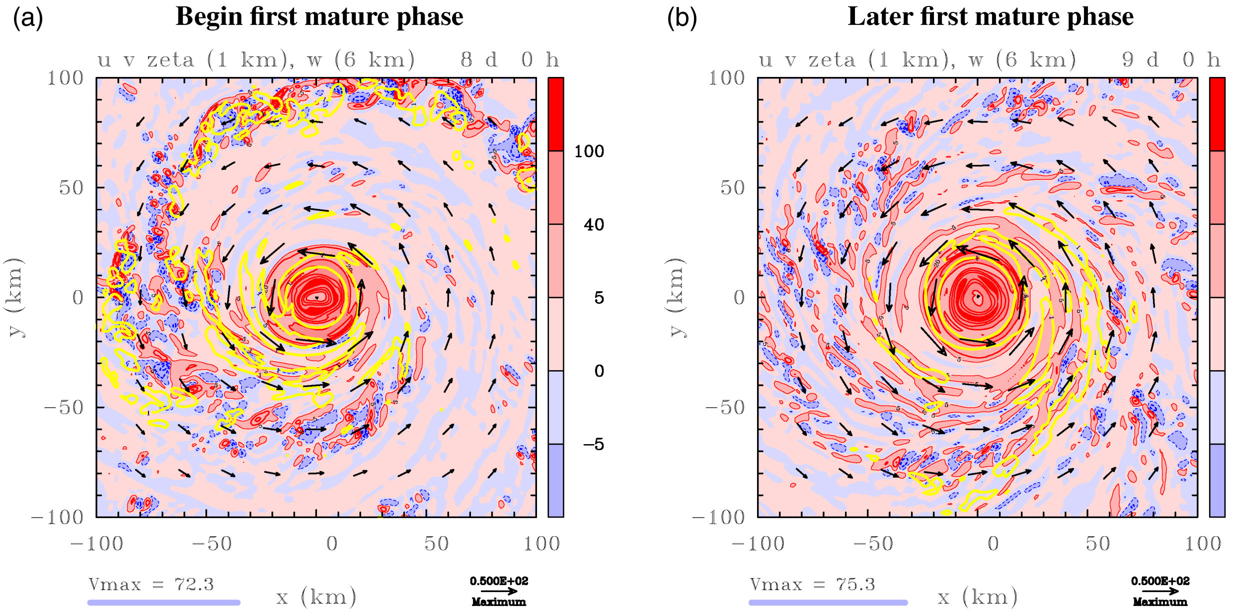
(a) Begin first mature phase

(b) Later first mature phase

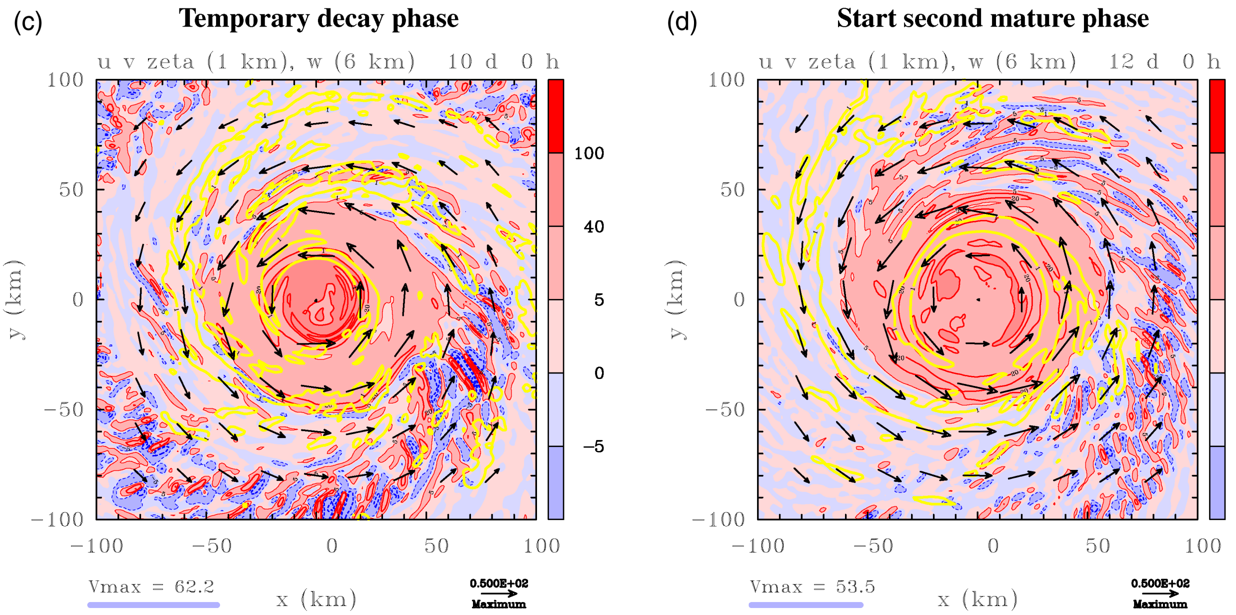
(c) Temporary decay phase

(d) Start second mature phase

FIGURE 2 Horizontal cross-sections of the vertical component of relative vorticity (shading) and wind vectors at (a) 8 days, (b) 9 days, (c) 10 days and (d) 12 days at 1 km altitude. In each panel are also shown contours of vertical velocity equal to 1 m·s^{-1} at a height of 6 km (yellow). Values for the shading of vertical vorticity are given in the colour bar, multiplied by 10^{-4}s^{-1}. For values greater than 5×10^{-4}s^{-1}, the red solid contours are relative vorticity at intervals of 2×10^{-3}s^{-1}, and below -5×10^{-4}s^{-1} the blue dashed contours have the same interval. The wind vectors are relative to the maximum reference vector (50 m·s^{-1}) at the bottom right, while the value of $V_{\max}$ (defined in Section 3) at a particular time is indicated by a thick light blue horizontal line with units of m·s^{-1} [Colour figure can be viewed at wileyonlinelibrary.com]

approximately circular core of high vorticity. The maximum vorticity, values $> 1 \times 10^{-2}$ s^{-1}, occur within an annular region inside the ring of convection at 6 km height. Beyond the inner ring of deep convection, most of the deep convection has become organized along three spiral bands, the two inner bands beginning at a radius of about 25 km to the southeast of the vortex centre. The outer one begins at a radius of about 40 km also to the southeast of the centre, but becomes most pronounced starting at the southwest of the centre and running clockwise to the northeast while progressively moving away from the centre. Away from these bands there are large regions free from deep convection.

Despite the tendency for the flow to become more and more axisymmetric with time during the RI phase, there remains an appreciable degree of asymmetry in the pattern of convection even at the first mature phase. This behaviour is consistent, of course, with that found in

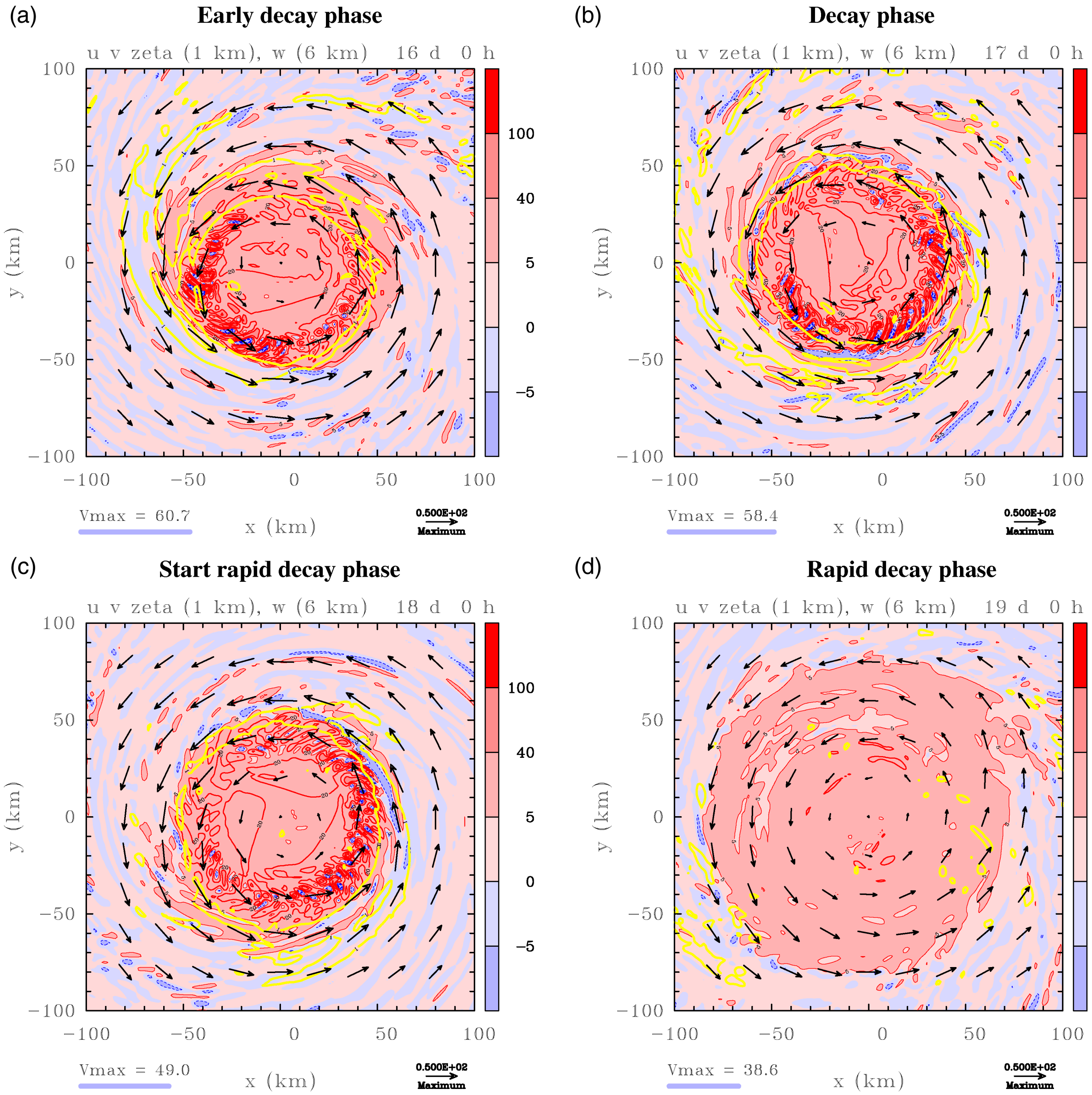

FIGURE 3 As Figure 2, but at times (a) 16 days, (b) 17 days, (c) 18 days and (d) 19 days [Colour figure can be viewed at wileyonlinelibrary.com]

previous simulations with somewhat coarser resolution (e.g., Wang, 2002; Nguyen *et al.*, 2008; Shin and Smith, 2008; Fang and Zhang, 2011) and in observations (Houze *et al.*, 2009; Molinari and Vollaro, 2010; Rogers *et al.*, 2013; Guimond *et al.*, 2016a), but is worth noting in the context of the present calculations.

While intensity fluctuations in terms of $V_{\max}$ are small during the first mature phase (Figure 1a), the vortex core steadily expands in terms of R_{Vmax} (Figure 1b). The expansion is manifest in Figure 2b as a radial expansion of the core of enhanced cyclonic vorticity compared with that in Figure 2a. As at 8 days, there remains an approximately annular region of deep convection within the region of enhanced vorticity, but its mean radius has increased compared with that at 8 days, consistent with the increase in R_{Vmax}. There is a noticeable difference in the spiral rainband structure between 8 and 9 days with a large increase in deep convection in the sector between southwest and eastnortheast, outside the inner convective ring, but the deep convection in the outermost band at 8 days has decayed. Nevertheless, vorticity anomalies associated with this convection still remain.

Figures 2c,d show the vorticity and vertical velocity fields at 10 days, roughly midway in the decline of

$V_{\max}$ after the first mature phase and at 12 days, which is near the start of the second mature phase following a subsequent intensification of $V_{\max}$ (Figure 1a). A prominent feature of both figures is the continued expansion of the core of enhanced vorticity, which by Stokes' theorem accounts for the expansion of the tangential wind field in the outer region of the vortex.

At 10 days, the decline in $V_{\max}$ is accompanied by a break in the ring of "eyewall convection" and this fragmentation continues for about a day, but a convective rain band complex develops beyond the ring and remains a dominant feature as the vortex reintensifies after 11 days (not shown). By 12 days (Figure 2d), when the vortex has re-intensified, the eyewall of deep convective cloud has almost re-consolidated into an annular ring, but with a somewhat larger mean radius than before. In contrast, the convective band complex has weakened somewhat and is no longer evident in all sectors. We show later that this convective band is an important feature during the weakening and subsequent re-intensification of the vortex between 9.5 and 12 days.

4.2 | Decay phase

Figure 3 shows the vorticity and vertical velocity fields at times during the decay phase, which begins after about 13 days. Figure 3a,b show the fields after 16 and 17 days, respectively. These are times when the decay rate is still relatively modest. The structures in the two panels are similar, each having a large core of enhanced relative vorticity, the strength of which declines rapidly beyond a radius of between 60 and 70 km. This behaviour is reflected in that of R_{gales} (Figure 1c), which reaches a plateau during the early decay period, but declines rapidly after 18 days when the vortex intensity begins to decay rapidly.

By 16 days (Figure 3a), the eyewall updraught at 6 km height has become rather large, around 50 km in mean radius, and fine-scale structures in the relative vorticity field have developed there on the inner edge of this updraught. These structures have largest amplitude along the southwestern semicircle and would suggest the presence of an instability on the inner edge of the eyewall. The occurrence of small patches of negative vorticity within these structures points to the tilting of horizontal vorticity into the vertical. It turns out that the eyewall updraught at lower altitudes is broken into localized structures with a similar horizontal scale to that of the vorticity structures (not shown).

One day later (Figure 3b), the eyewall updraught at 6 km height has become even larger, but remains ring-like. The small-scale vorticity structures remain, but are now largest in the semicircle centred to the southeast.

At 18 days (Figure 3c), the eyewall updraught at 6 km height has begun to break up. The small-scale vorticity structures persist, but are now largest in the semicircle centred to the east. Finally, by 19 days (Figure 3d), deep convective updraughts stronger than 1 m·s^{-1} at 6 km height have all but disappeared, as have the small-scale vorticity features at 1 km. What remains is a large and almost circular region of enhanced relative vorticity with radius on the order of 80 km and values exceeding 5×10^{-4} s^{-1}.

It is evident that the decay phase has a strong asymmetric component involving some form of eyewall instability. This instability would be a challenge to properly represent in an axisymmetric model. Dynamical and thermodynamical aspects of the decay process are discussed in Section 6.

5 | AZIMUTHALLY AVERAGED VIEW OF VORTEX EVOLUTION

Even though the evolution of the flow described above is intrinsically three-dimensional, as shown in Section 4, it is enlightening to examine the evolution of the azimuthally averaged flow fields. The azimuthally averaged view provides a link to the basic conceptual model of tropical cyclone dynamics and behaviour that goes back to Ooyama (1969). As noted in the previous section, the three-dimensional flow evolution prior to genesis and during the RI phase is quite similar to that described in Kilroy *et al.* (2017b). Thus, we confine the discussion here again to the two mature phases, which are separated by a temporary period of decay, and the final decay phase itself, which ends with a period of rapid decay. The decay phases, in particular, are phases of storm evolution which, as far as we are aware, have received comparatively little attention to date.

Figures 4 and 5 show radius–height cross-sections of the azimuthally averaged, 3 hr time-averaged tangential, radial and vertical velocity components at various times during the mature and decay phases. The corresponding averaged M-surfaces are shown with the averaged radial velocity fields. The times at which the figures are shown are indicated by thin vertical lines in Figure 1.

5.1 | Mature phase

Figures 4a,b show the radius–height cross-sections at 9 days, which is well within the first mature phase (Figure 1a). At this time, the mean updraught is narrow and the strongest part ($w > 1$ m·s^{-1}) is centred at a radius of 20 km. The maximum mean tangential velocity at this time is about 75 m·s^{-1} and it occurs at a radius

First mature phase near maximum intensity

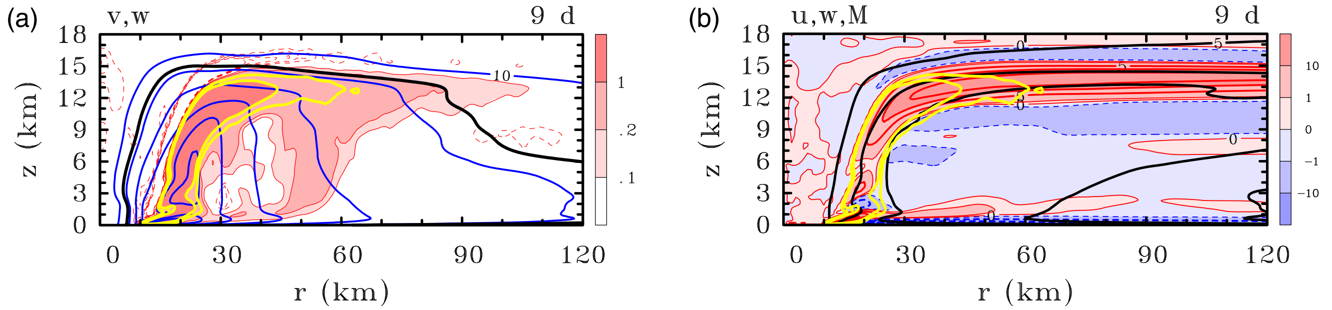

Midway during the first period of decay

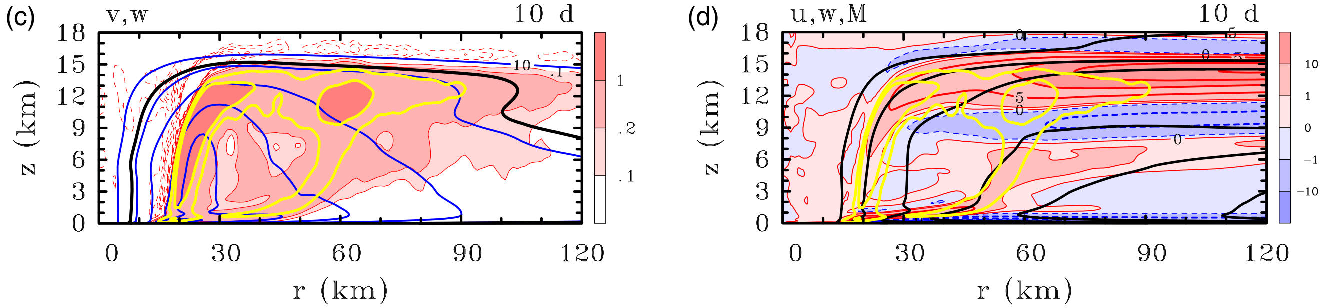

Start of the second mature phase

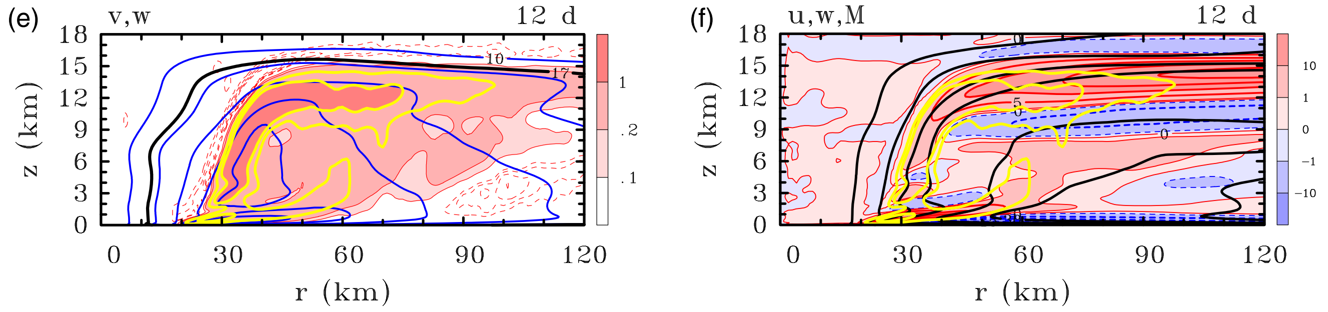

FIGURE 4 Vertical cross-sections of the azimuthally averaged, 3 hr time-averaged (a, c, e) tangential and (b, d, f) radial velocity components centred at various times: (a, b) 9 days, (c, d) 10 days, (e, f) 12 days. (a, c, e) - show contours and shading of the azimuth and time averaged vertical velocity. Contour intervals are as follows. Tangential velocity: blue contours every 5 m·s^{-1}. The bold black contour is the radius of gale-force tangential wind (17 m·s^{-1}), the outer portion of which provides a suitable measure of vortex size at different levels. Vertical velocity: thin red contours 0.1 m·s^{-1} and 0.2 m·s^{-1}, thick yellow contours are 0.5 and 1 m·s^{-1}, thin dashed red contours indicate subsidence at intervals of 0.02 m·s^{-1}. Shading is indicated on the side bar. (b, d, f) show contours and shading of the averaged radial velocity with contours of averaged absolute angular momentum (M. black) and the two yellow contours of the averaged vertical velocity superimposed. Contour intervals are as follows. Radial velocity: 5 m·s^{-1}, solid red contours positive, dashed blue contours negative, with intervals 1 m·s^{-1}. Shading is indicated on the side bar. Absolute angular momentum: black contours every 5×10^5 m^2 ·s^{-1} [Colour figure can be viewed at wileyonlinelibrary.com]

of 16 km and a height of 300 m (Figure 4a). As found in many previous studies, there is a shallow layer of strong frictionally driven inflow near the surface (Figure 4b). While it is hard to discern from this figure, the maximum inflow velocity is 35 m·s^{-1} and occurs very close to the surface at a radius of 19 km.

There is a shallow layer of strong outflow with maximum speed of 16 m·s^{-1} just above where the frictional inflow terminates, a shallow layer of inflow above that, and another local maximum of outflow just above this layer. These features are a part of a standing centrifugal recoil effect that appears to have been first described by Persing *et al.* (2013) and more recently documented in observations by Stern *et al.* (2020). This standing centrifugal wave forms as air having a supergradient tangential wind speed ascends out of the boundary layer and accelerates outwards, approximately conserving its absolute angular momentum as it does so. As the tangential wind speed of this air slows down, the air ultimately becomes subgradient and begins to accelerate inwards as it ascends

Early decay phase

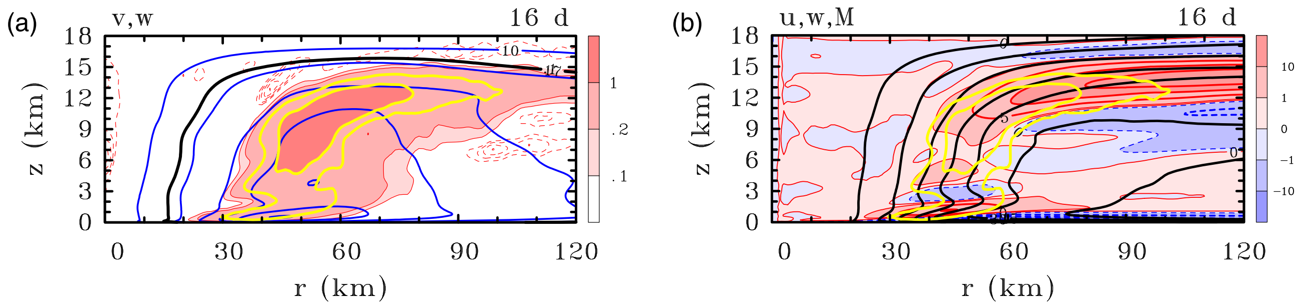

Decay phase

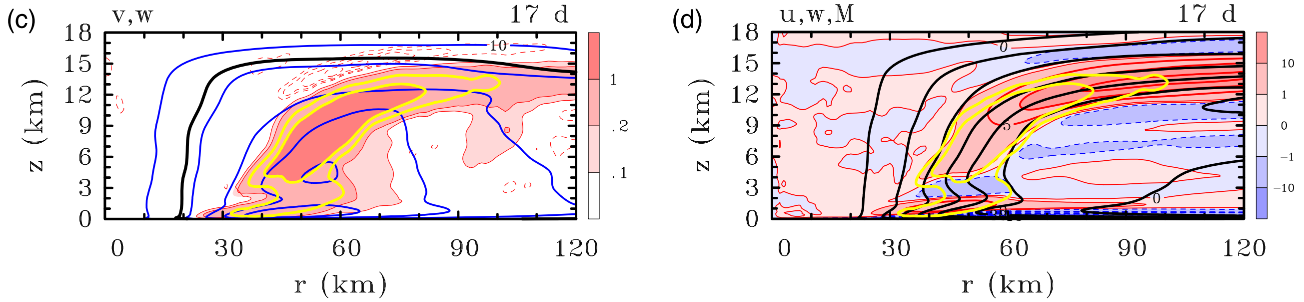

Start of rapid decay phase

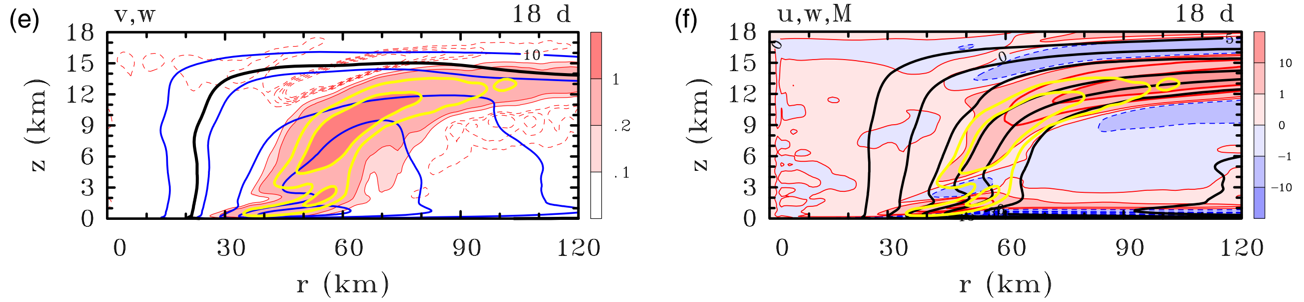

Rapid decay phase

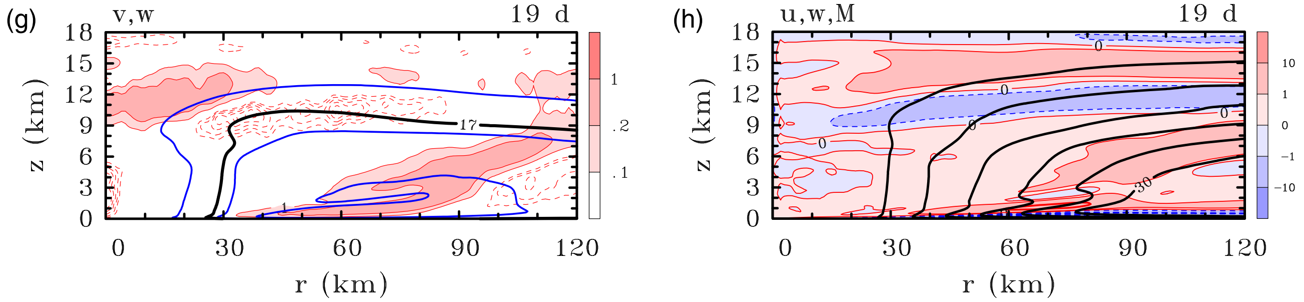

FIGURE 5 As Figure 4, but at times (a, b) 16 days, (c, d) 17 days, (e, f) 18 days, (g, h) 19 days [Colour figure can be viewed at wileyonlinelibrary.com]

into the eyewall. This wave appears first during the RI period (not shown) and it tends to be a persistent feature of the first mature phase, accounting for the second maximum of tangential wind at an altitude near 3 km.

The shallow layer of outflow, itself, extends radially as a tongue with mean radial velocity exceeding 1 m$\cdot$s^{-1} out to a radius of nearly 90 km. Assuming that, as in the classical model for vortex spin-up, mean absolute angular momentum, M, is approximately materially conserved, the outflow would indicate that the tangential wind speed in this tongue, and therefore at the top of the boundary layer, is already spinning down as M surfaces are advected outwards. This spin-down has consequences for the boundary-layer inflow and is an aspect of the boundary-layer control mechanism described by Kilroy *et al.* (2016) and in Sections 6.2 and 6.3 below.

Elsewhere in the low to mid-troposphere (below about 9 km) above the boundary layer, there is mostly weak inflow ($|u| < 1\,\mathrm{m\cdot s^{-1}}$).

The mean eyewall updraught is highlighted in each panel by the two yellow contours of mean vertical velocity, w, equal to 0.5 and $1\,\mathrm{m\cdot s^{-1}}$. As judged by the separation of either contour, at 9 days the updraught is quite narrow, less than 10 km wide, in the low to mid-troposphere. There it has only a small outward tilt with the centre axis at about 20 km radius up to about 6 km height, but the tilt increases with height above this level. The increasing tilt is accounted for by the progressively increasing strength of the radial outflow in the eyewall updraught above about 5.5 km in height.

Note the kink in both w contours of at a height of about 1.5 km. There is a localized maximum of strong ascent ($2.3\,\mathrm{m\cdot s^{-1}}$) below this height, at $z = 1.2$ km, which is indicative of dynamically forced ascent where the boundary-layer inflow terminates. The maximum value of w, $6.1\,\mathrm{m\cdot s^{-1}}$ at an altitude of 8.8 km, is a reflection of buoyantly forced ascent in the main eyewall updraught.

The main outflow layer occurs at altitudes between about 12 km and nearly 16 km (the approximate height of the tropopause in the ambient thermodynamic sounding). The maximum outflow velocity exceeds $18\,\mathrm{m\cdot s^{-1}}$ at the edge of the domain shown. Beyond the domain shown, the outflow velocity declines with increasing radius, as would be expected on the basis of continuity. As shown by Wang *et al.* (2020), the decline is brought about by an inward-directed mean agradient force in the outflow layer.

There are prominent layers of inflow sandwiching the upper-tropospheric outflow layer, the strongest one beneath the outflow in the height range of about 9–12 km has a maximum inflow of $3.3\,\mathrm{m\cdot s^{-1}}$ at a height of 10.3 km. These inflow layers have been the subject of recent investigations by Montgomery *et al.* (2020), Wang *et al.* (2020) and Wang and Smith (2021).

The M-surfaces show a characteristic inward-pointing nose near the top of the boundary-layer inflow and those between 15 and 30 km radius show an outward-pointing nose near the top of the low-level outflow layer (Figures 4b), features that may be understood in terms of the approximate material conservation of M above the boundary layer and the fact that, in the frictional boundary layer, the M-surfaces have a large positive vertical gradient on account of the frictional torque there.

5.2 | Temporary decay and reintensification phase

Figures 4c,d show the azimuthally averaged structure at 10 days, which is roughly midway during the first period of vortex decay. Now the maximum mean tangential velocity is $62\,\mathrm{m\cdot s^{-1}}$ and the radius at which it occurs has moved 5 km outwards since 9 days.

Three particular changes stand out in comparison with the fields one day earlier. One is the increase in the radial extent of ascent with a strengthening of the weaker secondary updraught near a radius of 50 km which was already seen at 9 days in Figure 4a. As seen in Figure 2c, the increase in ascent is a result of several convective bands that have built up outside the eyewall convection, but by 10 days, the eyewall has become fragmented, at least judged by the $1\,\mathrm{m\cdot s^{-1}}$ contour of vertical velocity. The maximum mean updraught in Figure 4c is much weaker than that in Figures 4a (only $3.1\,\mathrm{m\cdot s^{-1}}$ compared with $6.1\,\mathrm{m\cdot s^{-1}}$), but it occurs 1 km higher at 9.8 km.

The second prominent change is a substantial reduction of the radial inflow in the low to mid-troposphere, which is now largely confined to radii beyond 60 km and below 5 km height, with mostly outflow at smaller radii, at least above the boundary layer (Figure 4d). The maximum low-level inflow velocity has fallen to $24\,\mathrm{m\cdot s^{-1}}$, but the radius at which the maximum occurs has increased to 24 km (5 km more than at 9 days). The third change is the strengthening of the upper-level outflow, which is associated with the increase in areal extent of convection.

A basis for understanding these three changes is obtained by recognizing the link between the strength of the boundary-layer inflow and the proportion of this air that cannot be ventilated by convection in the primary eyewall. This link is investigated in detail in Section 6.

5.3 | A new pathway to inner-core rainband formation

It is interesting to note also that the structures described above are different from those of a classical concentric eyewall which contracts inwards with time. First, the secondary mean updraught which forms in this simulation does not contract inwards. Moreover, as discussed above, its formation is linked to the low-level radial outflow which results from the unventilated part of the primary eyewall.

Comparison with Figures 2c,d reveals that the mean updraught seen in Figures 4c–f is part of a transient spiral rainband complex which forms around this time. These inner-core rainband structures evolve in ways that appear to resemble vortex Rossby waves (retrograde azimuthal propagation relative to local tangential wind and slow outward propagation that tends to stagnate in time, etc.), but we have not yet carefully analyzed their structure, nor their wave–mean and wave–wave interaction effects.

The formation of these inner-core rainbands (and the corresponding mean updraught) is different from that of a classical secondary eyewall (e.g., Willoughby *et al.*, 1984; Huang *et al.*, 2018) and to our knowledge is a pathway that has not been described previously. In essence, this pathway is associated with the inability of the primary eyewall to evacuate the mass that is converging in the boundary layer, whereupon the excess mass flows radially outwards to trigger convection at a larger radius.

The question remains, of course, of why a classical secondary eyewall does not form in this simulation. Based on our experience using CM1 and the simple warm rain (Kessler) option, classical secondary eyewalls in three dimensions are not common. However, recent work has discovered a plausible path to secondary eyewall formation in three-dimensional CM1 solutions using simpler physics options and these solutions have been analyzed and compared against the more complex warm-rain option in a recently submitted manuscript (Persing and Montgomery, personal communication). That work found that the incorporation of pseudo-adiabatic thermodynamics supported the formation of a plausible secondary eyewall, which contracted inwards and merged with the primary eyewall.

5.4 | Decay phase

Figure 5 shows radius–height cross-sections like those in Figure 4, but during the decay phase. As in the mature phases, the maximum tangential wind speed occurs within the shallow surface-based layer of strong inflow (e.g., radial wind speeds exceeding 4 m·s^{-1} in magnitude). This feature is significant because it is within the layer influenced by surface friction and, as noted in the Introduction, it is found in observations, at least in intensifying and mature storms.

The cross-sections in Figure 5 further illustrate the weakening and radial spread of the inner-core convection during the decay phase. A prominent feature in Figures 5b,d,f,h is that the *M*-surfaces are moving outwards just above the boundary layer on account of a positive radial wind component there. This outflow must be a consequence of the inability of deep convection to ventilate mass at the rate that it is converging in the boundary layer (Kilroy *et al.*, 2017b; Smith and Wang, 2018). The reasons for the progressive outward expansion of the radii of forced ascent and the subsequent weakening of the vortex core are discussed below in Section 6.

The eyewall becomes progressively more tilted during the decay phase as it moves steadily outwards from the centre (Figures 5a,c,e,g). By 19 days, a region of strong subsidence has developed in the upper troposphere just above the tilted eyewall updraught leading to a local thermally indirect overturning circulation there (Figures 5g). At this time, the radial flow through much of the troposphere is outwards (Figures 5h) and the transverse circulation has essentially collapsed. This latter feature is clearly evident also in the horizontal cross-section in Figure 3d, where deep convection is virtually non-existent.

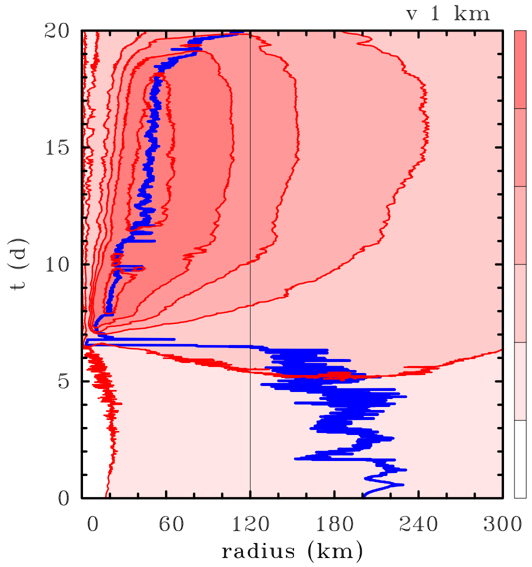

FIGURE 6 Hovmöller plot of the azimuthally averaged tangential velocity component (red contours and shading) at a height of 1 km out to 20 days. Also shown is the radius of the azimuthally averaged maximum tangential wind (blue curve). Red contours are every 17 m·s^{-1} [Colour figure can be viewed at wileyonlinelibrary.com]

6 | INTERPRETATIONS

As pointed out by Kilroy *et al.* (2016) (p. 493), the tight coupling between the flow above the boundary layer and that within the boundary layer makes it impossible, in general, to present simple cause and effect arguments to explain tropical cyclone behaviour. The best that one can hope to do is to articulate the individual elements of the coupling. In essence, these elements would represent a set of coupled mechanisms. In this section we show that an extension of the ideas developed in Kilroy *et al.*, can be applied to interpret the vortex behaviour described in Sections 3 to 5.

To provide a context for such an interpretation, we examine first a series of Hovmöller diagrams showing the evolution of certain low-level velocity fields together with the vertical velocity at a height of 6 km. We go on then to examine specific aspects of the boundary layer itself (Section 6.2), before discussing the coupling of the boundary layer with the flow above it (Section 6.3).

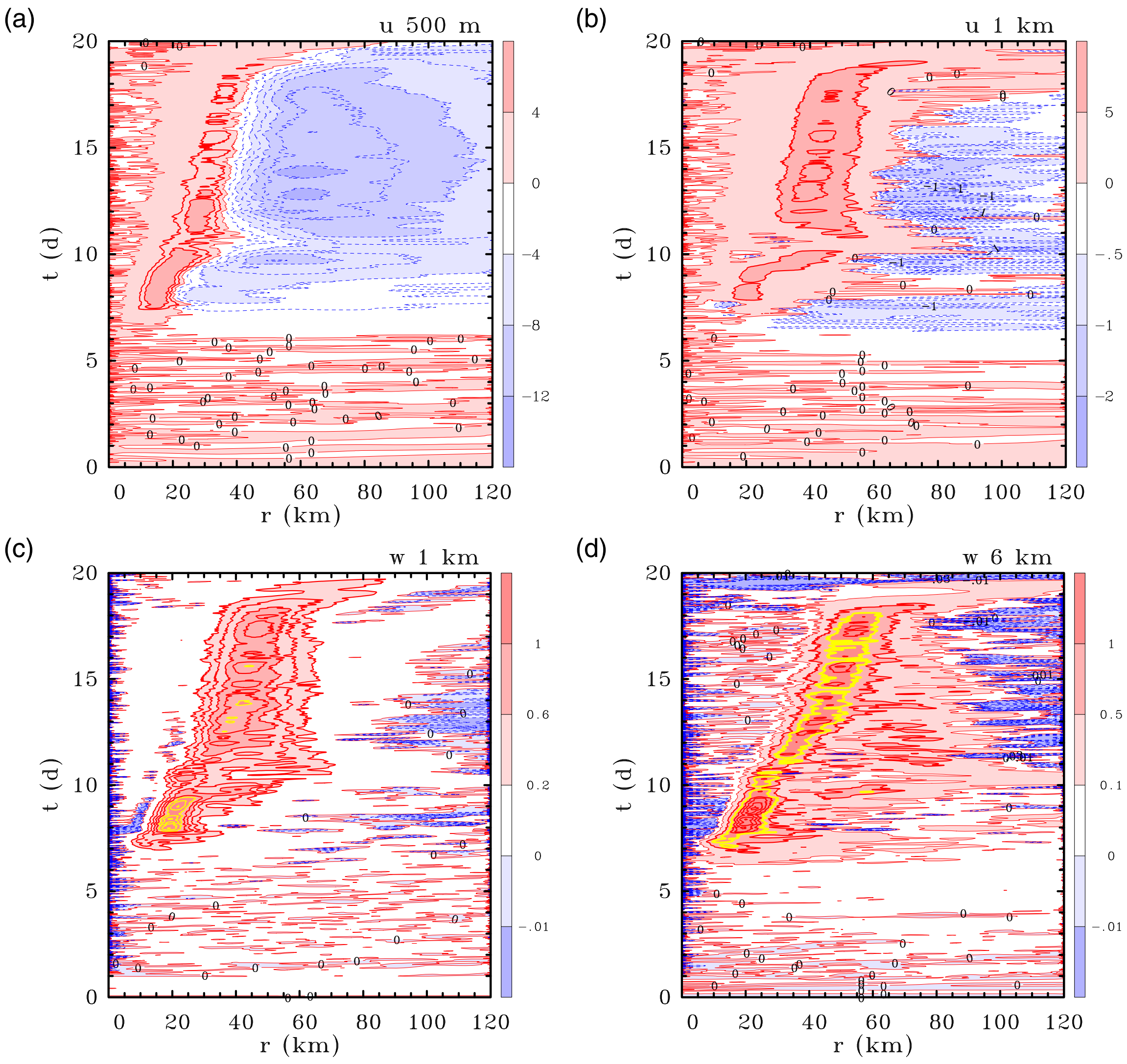

FIGURE 7 Hovmöller plots of the azimuthally averaged radial velocity component at heights of (a) 500 km and (b) 1 km, and vertical velocity at heights of (c) 1 km and (d) 6 km. Units are m s^{-1}. The yellow contour in (c, d) highlights values of vertical velocity larger than 1 m·s^{-1} [Colour figure can be viewed at wileyonlinelibrary.com]

6.1 | Low-level kinematics and mid-level vertical motion

Figure 6 shows a Hovmöller plot of the azimuthally averaged tangential velocity component at a height of 1 km, which is nominally at the top of the frictional boundary layer. The figure shows succinctly the sharp contraction of the velocity maximum at about 6.5 days and the subsequent expansion from a little after 7 days including the late RI phase, the second mature phase and the decay phase. This behaviour is similar to that of $V_{\max}$ and $R_{V\max}$ shown in Figures 1a,b. Seen also is the early expansion and subsequent contraction of R_{gales} (the contour with tangential wind speed equal to 17 m·s^{-1}).

Figure 7 shows Hovmöller diagrams of the similarly averaged radial velocity component at heights of 1 km near the top of the frictional boundary layer and 500 m, which is within the boundary layer, and the vertical velocity component at heights of 1 and 6 km. The behaviour of all fields is similar to that shown in Kilroy *et al.* (2016), suggesting that such behaviour is generic.

Within the boundary layer (Figure 7a), the flow is inwards except in a narrow strip at small radii where it is outwards, a indication of a localized "suction effect" by the eyewall convection. For most of the time, both the maximum inflow and maximum outflow as well as the dividing line separating inflow and outflow move radially outwards with time. This outward movement is particularly pronounced during the first period of vortex weakening between about 9.5 and 11 days (Figure 1a) and as the vortex rapidly decays beyond 18 days. Both of these periods are ones during which the inflow markedly weakens.

At the top of the boundary layer (Figure 7b), there is a narrow strip of outflow approximately co-located with the updraught shown in Figure 7c, and generally inflow beyond this strip, although there is a brief period between about 10 and 11 days when the outflow extends relatively far outwards. After 18 days as the vortex rapidly decays, there is outflow at most if not all radii.

The vertical velocity at 1 km height (Figure 7c) shows a narrow, but intense updraught emerging from the boundary layer with weak subsidence into the boundary layer at larger radii. This updraught is essentially the "eyewall" updraught. Beyond about 7 days, the radial location of the maximum vertical velocity increases progressively with time. At 6 km height (Figure 7d), the pattern of vertical motion is similar, but the eyewall updraught is a little broader and the maximum is further outwards than at 1 km, a reflection of the outward slope of the eyewall.

6.2 | Boundary-layer dynamics

Low-level inflow feeding into the developing inner-core deep convection is driven in part by the convection itself, which might be described as a "suction effect", and in part by the frictionally induced convergence associated with boundary-layer dynamics. Because the boundary-layer dynamics are intrinsically nonlinear in the inner region of the vortex, it is not possible to directly isolate the separate effects of the two processes leading to low-level inflow (Smith and Montgomery, 2015, p. 3027; Montgomery and Smith, 2017a; 2017b). To circumvent this problem, Kilroy *et al.* (2016) used an indirect method to isolate and estimate the boundary-layer-induced inflow and thereby the degree of control exerted by the boundary layer on the vortex evolution. In this method, they compared the azimuthally averaged velocity fields derived from the three-dimensional numerical model simulation with those of a simple, steady[3], axisymmetric, slab boundary-layer model driven by the time-dependent, azimuthally averaged tangential wind field at a height of 1 km obtained from the numerical model. The ability of the slab boundary-layer model to produce a radial distribution of vertical motion close to that in the time-dependent numerical model provides an effective measure of the degree to which boundary-layer dynamics are determining the low-level inflow. Kilroy *et al.*, showed that there was good qualitative agreement between the two sets of velocity fields, except near and beneath the eyewall updraught, and concluded that the boundary layer was the dominant mechanism in producing the inflow, except in the vicinity of the eyewall updraught itself.

While the expansion of the vortex core in the present calculation is consistent with the ideas of boundary-layer control discussed by Kilroy *et al.* (2016), an explanation for the temporary decay and re-intensification of the vortex between 9.5 and 12 days requires consideration of internal processes inside and near R_{Vmax}, where, as noted above, boundary-layer dynamics may not be wholly applicable. We return to this issue in Section 6.4.

6.3 | Boundary-layer coupling

According to classical balance vortex theory (e.g., Shapiro and Willoughby, 1982), the strength and geometrical configuration of the secondary circulation above the boundary layer is forced by the spatial distribution of diabatic heating rate throughout the troposphere together with the vertical motion at the top of the boundary layer. In turn, the vertical motion at the top of the boundary layer itself is determined largely by boundary-layer dynamics, the possible exception being beneath and near the eyewall updraught as explained above.

At radii where there is inflow just above the boundary layer and where the vertical motion at the top of the boundary layer is relatively weak, the tangential wind at that level will increase as absolute angular momentum surfaces are drawn inwards. Assuming that gradient wind balance prevails at this level, the local radial pressure gradient will increase also. According to boundary-layer theory, this pressure gradient will be transmitted instantaneously through the boundary layer to locally accelerate the inflow, thereby accentuating the boundary-layer convergence and ascent at the top of the boundary layer at inner radii.

Because the diabatic heating rate depends strongly on the thermodynamic properties of the ascending air and because the pattern of ascent is strongly tied to the dynamics of the boundary layer, the boundary layer exerts a strong influence on the evolution of the vortex. This influence is incorporated in the concept of *boundary-layer control* as articulated by Kilroy *et al.* (2016), a concept that is supported by the present calculations.

While the boundary-layer control mechanism as described above is based on axisymmetric reasoning, we have shown in Figure 2 that the decay phase is accompanied by strongly asymmetric processes that break up the contiguous eyewall updraught and lead in part to the formation of banded vorticity–convective structures. A more complete understanding of the decay phase of the vortex life cycle should incorporate these asymmetric processes and will be the topic of a future paper.

---

[3] The justification for using a steady boundary-layer model is that the boundary layer is a relatively shallow layer that can be expected to respond rapidly to the flow above it.

6.4 | Ventilation of the boundary-layer inflow

Many previous theories of tropical cyclone intensification, including Charney and Eliassen (1964)'s articulation of Conditional Instability of the Second Kind, Ooyama (1969)'s deductions from his pioneering three-layer hurricane model, and Emanuel (1997)'s intensification theory based on the WISHE[4] feedback mechanism, were based on the premise that all the mass converging in the boundary layer would ascend in deep convection. However, such an assumption is not supported by three-dimensional simulations with convection-permitting models, including the present one. Such simulations show that the ability of the aggregate of deep convection to ventilate the boundary layer, that is, to remove the mass converging in the boundary layer and transport it to the upper troposphere, cannot be taken for granted. Indeed, these simulations indicate a relentless mismatch between the mass flux exiting the boundary layer and the cloud-base mass flux associated with deep convection, due presumably to the stochastic nature of the convection. Although deep convection itself draws into it air from low levels, the calculations of Kilroy *et al.* (2016) indicate that, at least beyond the eyewall updraught, the low-level inflow is primarily controlled by boundary-layer dynamics.

While balance theory does not apply within the boundary layer, it should be a reasonable first approximation in the lower troposphere above the boundary layer (e.g., Willoughby, 1979; Bui *et al.*, 2009) and beyond the eyewall updraught (Montgomery *et al.*, 2020; Wang *et al.*, 2020). In this case, the ability of the convectively driven secondary circulation to ventilate the boundary layer depends on the spatial gradients of diabatic heating rate associated with the convection. As noted above, the diabatic heating rate depends to a first approximation on the vertical velocity as well as the θ_e of the air ascending out of the boundary layer. In this way, the boundary layer has a strong influence on the spatial structure and magnitude of the heating rate.

If the convection is strong enough to ventilate more mass than is supplied by the boundary layer, it will draw air inwards above the boundary layer, converging the M-surfaces there to spin up the tangential flow at the top of the boundary layer. Then, the boundary-layer inflow will increase, thereby increasing the upflow offered to the convection and, assuming that the spatial gradients of heating rate do not change during this period of spin-up, bringing the mass inflow closer to the mass being drawn upwards by the convection. As a result, the inflow above the boundary layer will decrease, as will the rate at which the tangential wind at the top of the boundary layer increases. Of course, in reality, the spatial gradients of heating rate will change also because of the strong coupling of conditions above the boundary layer with those in the boundary layer itself.

If the convection for some reason decreases in strength, so that the aggregate mass flux it draws upwards decreases, or if the boundary layer inflow increases because, for example, the radial pressure gradient at its top and therefore within it increases, it is conceivable that the convection may no longer be able to ventilate all the mass converging in the boundary layer. In this case, the residual mass will flow outwards just above the boundary layer.

If vertical velocities are small enough, the radial flow will advect the M-surfaces outwards and the vortical flow at the top of the boundary layer will spin down. Then, the boundary-layer inflow will weaken until, possibly, the convection is again able to draw mass upwards at a rate that is greater than the supply from the boundary layer, so that inflow ensues at the top of the boundary layer leading again to spin-up.

If the vertical velocities out of the boundary layer are not small enough, M-surfaces above the boundary layer can move inwards on account of the vertical advection of M from the boundary layer and the vortex may locally spin up there. This may happen, of course, only at radii where the tangential velocity in the boundary layer is larger than that above.

The ideas outlined above are useful for interpreting aspects of the flow evolution depicted in Figures 1 and 6. To underpin the discussion, we show in Figure 8a time series of the difference in the azimuthally averaged radially integrated mass flux between heights of 6 and 1 km, ΔM_{flux}, as a function of the radius of integration, R_{int}. Specifically,

$$\Delta M_{\text{flux}} = 2\pi \int_0^{R_{\text{int}}} [< \rho w >_{z=6\ \text{km}} - < \rho w >_{z=1\ \text{km}}] r\, \mathrm{d}r, \tag{1}$$

where $< \rho w >$ is the azimuthally averaged vertical mass flux with ρ the air density, w the vertical velocity and r the radius. This equation constitutes the "ventilation diagnostic" referred to in the abstract and elsewhere. Figure 8 shows also the 0.5 m·s^{-1} contours of vertical velocity at the two heights. Positive values of ΔM_{flux} indicate times and radii of integration at which the mass flux at 6 km exceeds that emerging from the boundary layer at a height of 1 km. These are times when deep convection is more than able to ventilate the mass converging in the boundary layer. On the other hand, negative values of ΔM_{flux} indicate times and radii of integration at which the convection is too weak to ventilate all the mass converging in the boundary layer. The fraction of mass not ventilated flows outwards just above the inflow layer and, as we saw in Figure 4d, this air may be ventilated by convection at larger radii.

---

[4] Wind Induced Surface Heat Exchange.

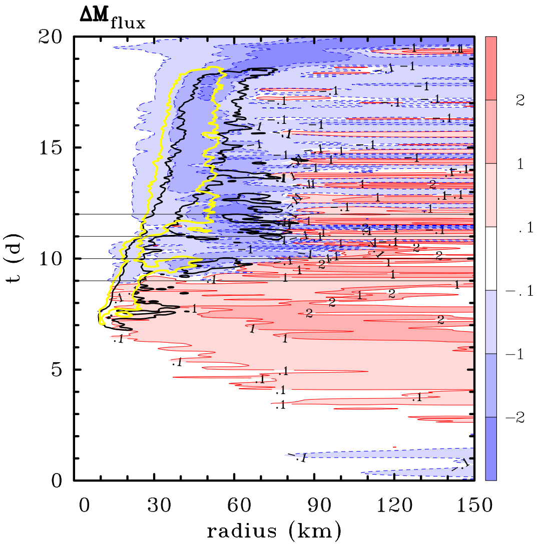

FIGURE 8 Hovmöller plot of the ventilation diagnostic, Equation (1), i.e., the azimuthally averaged radially integrated vertical mass flux difference between heights of 6 and 1 km as a function of the integration radius. R_{int} in Equation (1). Contour values on the ordinate should be multiplied by 10^9kg s^{-1}. Also shown are 0.5 m·s^{-1} contours of the azimuthally averaged vertical velocity at a height of 1 km (yellow) and 6 km (black). The thin horizontal black lines highlight four particular times referred to in the text [Colour figure can be viewed at wileyonlinelibrary.com]

Important features to note in Figure 8 are:

- Until almost 9 days, that is, during the RI phase and early maturity, $\Delta M_{\mathrm{flux}} > 0$ for all values of R_{int}. During this early time there is mostly inflow in the low to mid-troposphere as exemplified by Figure 4b but, as noted in Section 5.1, even at 9 days, a shallow tongue of radial outflow has developed just above the surface-based inflow layer. Animations of fields akin to those Figure 4b, but without time averaging, show that the *M*-surfaces are continuing to move slowly inwards in this tongue of outflow, indicating a vertical transfer of *M* from the inflow layer. Recall that, as exemplified also by Figure 4b, the *M*-surfaces have an inward-pointing nose within the inflow layer indicating that the maximum tangential wind speed resides there.
- At 9 days, ΔM_{flux} has just become negative in the mean eyewall updraught and shortly after 9 days the radius R_{int} beyond which ΔM_{flux} becomes positive increases sharply. Just before 9.5 days, the 0.5 m·s^{-1} contour of vertical velocity extends rapidly outwards, a reflection of the formation of the secondary updraught feature beyond the inner eyewall updraught seen in Figure 4c. As noted in Section 5, this feature is a consequence of the outer convective band seen in Figure 2c. This feature is evident also in Figure 8 by the closed 0.5 m·s^{-1} contour of vertical velocity at a slightly larger radius. It is clear now that the outer convective band is being fed by air that was unable to be ventilated by the eyewall convection itself.
- Between 10 and 11 days, as the vortex continues to decay after the first mature phase (Figure 1a), the radius beyond which R_{int} first becomes positive extends beyond 110 km. In this period, the eyewall updraught at 1 km becomes quite narrow and, as noted in Section 4.1, it is broken in azimuth.
- As the vortex re-intensifies, there is a sharp increase in the width of the mean eyewall updraught at a height of 1 km at about 11.5 days, an increase that is preceded a few hours earlier by a pulse of increased ascent at this level between 40 and 50 km. Again there are frequent periods with closed 0.5 m·s^{-1} contours of vertical velocity beyond the eyewall updraught that are most evident up to about 14 days. These periods are ones in which $\Delta M_{\mathrm{flux}} > 0$ at some radius inside 150 km. At other times when the outer convection is weaker, ΔM_{flux} is never positive inside this radius.
- Beyond 11 days until well into the final decay phase, the outer radius of the 0.5 m·s^{-1} contour of mean vertical velocity at 1 km remains more or less constant, but the inner radius moves progressively outwards as the inner eyewall expands. At 6 km altitude, the width of the mean eyewall expands and the mean radius moves outwards until, soon after 18 days, deep convection ceases in an azimuthal mean sense and the eyewall updraught collapses (cf. Figure 3d). From about 14 days onwards, deep convection becomes progressively unable to ventilate the mass exiting the boundary layer and at many times ΔM_{flux} never becomes positive inside 150 km. After the eyewall updraught collapses, ΔM_{flux} is strongly negative inside 100 km radius.

In summary, during the first intensification phase, the developing eyewall updraught is more than able to ventilate the mass of boundary-layer air being supplied to it. During the first mature phase, this ability ceases and leads to some low-level outflow above the boundary layer which initiates deep convection in a band beyond the eyewall updraught. Subsequently the eyewall updraught weakens and the vortex undergoes a temporary period of decay followed by a re-intensification phase. This period of decay and reintensification is accompanied by a reorganization of deep convection in which the eyewall updraught reforms during a 6–8 hr period at a somewhat larger radius than before.

Aspects of the reorganization are illustrated by time series of R_{Vmax}, R_{Umin} and R_{WmaxL} during the period 9–12 days shown in Figure 9. Here, R_{Umin} and R_{WmaxL}

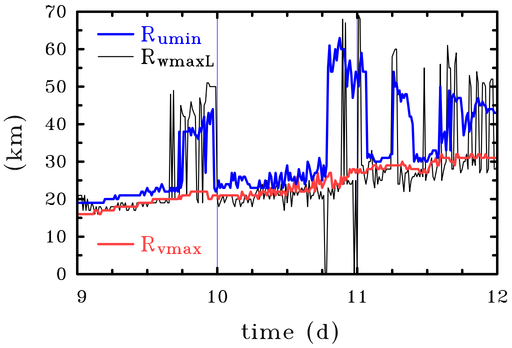

FIGURE 9 Time series of R_{Vmax} (red), R_{Umin} (blue) and R_{WmaxL} (black) over the period 9–12 days, during which there is a major reorganization of deep convection. The thin vertical blue line at 10 days is for reference only [Colour figure can be viewed at wileyonlinelibrary.com]

are the radii of maximum azimuthally averaged radial inflow and vertical velocity, respectively, the latter calculated up to an altitude of 3 km only. Notice the sharp increase of R_{Umin} at about 9.7 days and the large fluctuations in R_{WmaxL}. The latter are suggestive of a substantial change in the character of the moist convection just prior to the rapid increase of R_{Umin} a few hours later. Both quantities recover at about 10 days, but begin to fluctuate again just after 10.75 days. It is at about this time that the mean eyewall updraught below 3 km shifts outwards over a period of 6–8 hr from approximately 25 to 55 km radius. Subsequently, the large fluctuations in R_{Umin} and R_{WmaxL} become more persistent and sharp positive increases in these quantities are an indication that the roots of the outer band of deep convection are stronger collectively than those of the eyewall convection itself. During the entire three-day period, R_{Vmax} increases comparatively steadily, the largest rate of increase being during the 6–8 hr that the mean eyewall updraught below 3 km shifts outwards.

The reorganization of the deep convection is necessitated by the progressive inability of deep convection to ventilate the mass that is being ejected by the boundary layer. This inability is quantified by negative values of ΔM_{flux} and is presumably a reflection of, at least in part, the decreasing convective instability evident in the weakening maximum local vertical velocity after 10 days seen in Figure 1d. After the re-organization and brief period of re-intensification between 11 and 12 days, the mean eyewall updraught continues to expand and its mean radius increases. This updraught and the deep convection in spiral bands beyond it increasingly struggle to evacuate the mass being ejected by the boundary layer. Again, the decreasing convective instability suggested by the decline in w_{max} in Figure 1d would explain this struggling. During this later period, first the rainbands decay and then the eyewall updraught itself.

On short time-scales of an hour or less, there are significant fluctuations of ΔM_{flux} indicating that there is generally a mismatch between the rate of boundary-layer mass convergence and the rate at which this mass is being ventilated by deep convection. This mismatch provides an explanation for the rapid fluctuations in the evolution of V_{max} seen in Figure 1a. It provides an explanation also for the pulses of positive radial flow near the top of the boundary layer seen in Figure 4b. These pulses occur during periods of prolonged negative values of ΔM_{flux}.

The processes described above may operate also in realistic tropical cyclones and it is possible that they could be incorrectly interpreted as a result of ambient vertical wind shear, which is not present in the model discussed here.

7 | CONCLUSIONS

We have used a relatively high-resolution, three-dimensional, idealized numerical simulation of a tropical cyclone in a quiescent environment on an f-plane to explore some fundamental dynamical and thermodynamical aspects of the cyclone's life cycle in the framework of the rotating-convection paradigm. Since the simulation does not include an ambient flow and has a homogeneous sea surface temperature, the intensity and structure changes that accompany the mature and rapid decay phases represent internal modes of vortex variability that need to be understood as a prerequisite to understanding observed or simulated tropical cyclone intensity change in more complex situations.

In the simulation, which lasts for 20 days and starts with a weak, axisymmetric, cloud-free vortex in thermal wind balance, the vortex undergoes a life cycle that includes a gestation period leading to genesis, a rapid intensification phase, a first mature phase followed by a transient decay and re-intensification phase, a second mature phase and a final rapid decay phase. It was found that, during most of the life cycle, the flow evolution is generally asymmetric, although to a first approximation, much of the evolution can be understood conceptually in terms of an azimuthally averaged framework that implicitly includes both mean and eddy processes.

Vortex evolution during much of the life cycle, especially in the mature and decay phases, can be interpreted in terms of the boundary-layer control mechanism, first explored by Kilroy *et al.* (2016), and a new ventilation diagnostic characterizing the ability of deep convection within a given radius to evacuate the mass of air that is ascending out of the boundary layer within that radius. The boundary-layer control mechanism provides an explanation for the gradual expansion of the inner core of the vortex, while the ventilation diagnostic highlights the increasing difficulty of deep convection to ventilate the amount of air that exits the boundary layer within a particular radius. The ultimate rapid decay of the vortex is a result of the unventilated air flowing radially outwards in the lower troposphere, which on the basis of the approximate material conservation of mean absolute angular momentum leads to rapid spin-down and vortex collapse. This decay process is independent of the influence of ambient vertical shear and it is possible that it operates in realistic long-lived tropical cyclones, yet may be incorrectly interpreted as a result of ambient vertical wind shear.

The transient decay and re-intensification phase is not associated with an eyewall replacement cycle, but rather with a process in which the eyewall temporally fragments while a rainband complex forms beyond it. This process is shown to be an example of the interplay between the boundary layer and ventilation, but seems not to have been described previously, either in theoretical or observational studies. Like the rapid decay process described above, this process may operate also in realistic tropical cyclones and, again, might be incorrectly interpreted as a result of ambient vertical wind shear.

The results of this study support recent work suggesting that, even in a quiescent environment on an f-plane, isolated tropical cyclone vortices are intrinsically transient systems and never reach a globally steady state.

AUTHOR CONTRIBUTIONS

Roger K. Smith: Gerard Kilroy: conceptualization; formalAnalysis; Software; writingReviewEditing. **M. T. Montgomery:** conceptualization; writingReviewEditing.

ACKNOWLEDGEMENTS

MTM acknowledges the support of ONR grants N0001417WX00336 and N0001420WX01473 and the U.S. Naval Postgraduate School. GK acknowledge financial support for tropical cyclone research from the German Research Council (Deutsche Forschungsgemeinschaft) under grant KI-2248. The views expressed herein are those of the authors and do not represent sponsoring agencies or institutions. Open Access funding enabled and organized by Projekt DEAL. WOA Institution: LUDWIG-MAXIMILIANS-UNIVERSITAET MUNCHEN Blended DEAL: Projekt DEAL

ORCID

Roger K. Smith https://orcid.org/0000-0002-3668-1608

REFERENCES

Anthes, R.A. (1974) The dynamics and energetics of mature tropical cyclones. *Reviews of Geophysics*, 12, 495–522.

Bell, M.M. and Montgomery, M.T. (2008) Observed structure, evolution, and potential intensity of category 5 hurricane *Isabel* (2003) from 12 to 14 September. *Monthly Weather Review*, 136, 2023–2046.

Bister, M. and Emanuel, K.A. (1998) Dissipative heating and hurricane intensity. *Meteorology and Atmospheric Physics*, 50, 233–240.

Bryan, G.H. (2012) Effects of surface exchange coefficients and turbulence length scales on the intensity and structure of numerically simulated hurricanes. *Monthly Weather Review*, 140, 1125–1143.

Bryan, G.H. and Fritch, J.M. (2002) A benchmark simulation for moist nonhydrostatic numerical models. *Monthly Weather Review*, 130, 2917–2928.

Bryan, G.H. and Rotunno, R. (2009) Evaluation of an analytical model for the maximum intensity of tropical cyclones. *Journal of the Atmospheric Sciences*, 66, 3042–3060.

Bui, H.H., Smith, R.K., Montgomery, M.T. and Peng, J. (2009) Balanced and unbalanced aspects of tropical-cyclone intensification. *Quarterly Journal of the Royal Meteorological Society*, 135, 1715–1731.

Charney, J.G. and Eliassen, A. (1964) On the growth of the hurricane depression. *Journal of the Atmospheric Sciences*, 21, 68–75.

Črnivec, N., Smith, R.K. and Kilroy, G. (2015) Dependence of tropical cyclone intensification rate on sea surface temperature. *Quarterly Journal of the Royal Meteorological Society*, 142, 1618–1627.

Dunion, J.P. (2011) Rewriting the climatology of the tropical North Atlantic and Caribbean Sea atmosphere. *Journal of Climate*, 24, 893–908.

Emanuel, K.A. (1986) An air–sea interaction theory for tropical cyclones. Part I: steady state maintenance. *Journal of the Atmospheric Sciences*, 43, 585–604.

Emanuel, K.A. (1988) The maximum intensity of hurricanes. *Journal of the Atmospheric Sciences*, 45, 1143–1155.

Emanuel, K.A. (1995) The behavior of a simple hurricane model using a convective scheme based on subcloud-layer entropy equilibrium. *Journal of the Atmospheric Sciences*, 52, 3960–3968.

Emanuel, K.A. (1997) Some aspects of hurricane inner-core dynamics and energetics. *Journal of the Atmospheric Sciences*, 54, 1014–1026.

Fang, J. and Zhang, F. (2011) Evolution of multiscale vortices in the development of hurricane *Dolly* (2008). *Journal of the Atmospheric Sciences*, 68, 103–122.

Guimond, S.R., Heymsfield, G.M. and Turk, F.J. (2010) Multiscale observations of hurricane *Dennis* (2005): the effects of hot towers on rapid intensification. *Journal of the Atmospheric Sciences*, 67, 633–654.

Guimond, S.R., Reisner, J., Marras, S. and Giraldo, F. (2016a) The impacts of dry dynamic cores on asymmetric hurricane intensification. *Journal of the Atmospheric Sciences*, 73, 4661–4684.

Guimond, S.R., Heymsfield, G.M., Reasor, P.D., and Didlake Jr. A.C. (2016b) The rapid intensification of Hurricane Karl (2010): New remote sensing observations of convective bursts from the Global Hawk platform. *Journal of the Atmospheric Sciences*, 73, 3617–3639.

Hakim, G.J. (2011) The mean state of axisymmetric hurricanes in statistical equilibrium. *Journal of the Atmospheric Sciences*, 68, 1364–1376.

Hogan, R. and Bozzo, A. (2018) Nonlinear response of a tropical cyclone vortex to prescribed eyewall heating with and without surface friction in TCM4: implications for tropical cyclone intensification. *Journal of Advances in Modeling Earth System*, 10, 1990–2008.

Houze, R.A., Lee, W.C. and Bell, M.M. (2009) Convective contribution to the genesis of hurricane *Ophelia* (2005). *Monthly Weather Review*, 137, 2778–2800.

Huang, Y.-H., Wu, C.-C. and Montgomery, M.T. (2018) Concentric eyewall formation in typhoon *Sinlaku* (2008). Part III: horizontal momentum budget analyses. *Journal of the Atmospheric Sciences*, 75, 3541–3563.

Jakob, C., Singh, M.S. and Jungandreas, L. (2019) Radiative convective equilibrium and organised convection – an observational perspective. *Journal of Geophysical Research*, 124, 5418–5430.

Kepert, J.D. (2006a) Observed boundary-layer wind structure and balance in the hurricane core. Part I. Hurricane *Georges*. *Journal of the Atmospheric Sciences*, 63, 2169–2193.

Kepert, J.D. (2006b) Observed boundary-layer wind structure and balance in the hurricane core. Part II. Hurricane *Mitch*. *Journal of the Atmospheric Sciences*, 63, 2194–2211.

Kilroy, G. and Smith, R.K. (2012) A numerical study of rotating convection during tropical cyclogenesis. *Quarterly Journal of the Royal Meteorological Society*, 139, 1255–1269.

Kilroy, G., Smith, R.K. and Montgomery, M.T. (2016) Why do model tropical cyclones grow progressively in size and decay in intensity after reaching maturity?. *Journal of the Atmospheric Sciences*, 73, 487–503.

Kilroy, G., Smith, R.K. and Montgomery, M.T. (2017a) Tropical low formation and intensification over land as seen in ECMWF analyses. *Quarterly Journal of the Royal Meteorological Society*, 143, 772–784.

Kilroy, G., Smith, R.K. and Montgomery, M.T. (2017b) A unified view of tropical cyclogenesis and intensification. *Quarterly Journal of the Royal Meteorological Society*, 143, 450–462.

Mapes, B.E. (1993) Gregarious tropical convection. *Journal of the Atmospheric Sciences*, 50, 2026–2037.

Mapes, B.E. and Houze, R.A. (1995) Diabatic divergence profiles in Western Pacific mesoscale convective systems. *Journal of the Atmospheric Sciences*, 52, 1807–1828.

Mapes, B.E. and Zuidema, P. (1996) Radiative-dynamical consequences of dry tongues in the tropical troposphere. *Journal of the Atmospheric Sciences*, 53, 620–638.

Molinari, J. and Vollaro, D. (2010) Rapid intensification of a sheared tropical storm. *Monthly Weather Review*, 138, 3869–3885.

Montgomery, M.T., Kilroy, G. and Smith, R.K. (2020) Contribution of mean and eddy momentum processes to tropical cyclone intensification. *Quarterly Journal of the Royal Meteorological Society*, 146, 3101–3117.

Montgomery, M.T. and Smith, R.K. (2014) Paradigms for tropical cyclone intensification. *Australian Meteorological and Oceanographic Society Journal*, 64, 37–66.

Montgomery, M.T. and Smith, R.K. (2017a) On the applicability of linear, axisymmetric dynamics in intensifying and mature tropical cyclones. *Fluids*, 2, 69

Montgomery, M.T. and Smith, R.K. (2017b) Recent developments in the fluid dynamics of tropical cyclones. *Annual Review of Fluid Mechanics*, 49, 541–574.

Montgomery, M.T., Zhang, J.A. and Smith, R.K. (2014) An analysis of the observed low-level structure of rapidly intensifying and mature hurricane *Earl* (2010). *Quarterly Journal of the Royal Meteorological Society*, 140, 2132–2146.

Nguyen, V.S., Smith, R.K. and Montgomery, M.T. (2008) Tropical-cyclone intensification and predictability in three dimensions. *Quarterly Journal of the Royal Meteorological Society*, 134, 563–582.

Nolan, D.S. (2007) What is the trigger for tropical cyclogenesis?. *Australian Meteorological Magazine*, 56, 241–266.

Ooyama, K.V. (1969) Numerical simulation of the life cycle of tropical cyclones. *Journal of the Atmospheric Sciences*, 26, 3–40.

Ooyama, K.V. (1982) Conceptual evolution of the theory and modeling of the tropical cyclone. *Journal of the Meteorological Society of Japan*, 60, 369–380.

Persing, J., Montgomery, M.T., McWilliams, J. and Smith, R.K. (2013) Asymmetric and axisymmetric dynamics of tropical cyclones. *Atmospheric Chemistry and Physics*, 13, 12299–12341.

Persing, J., Montgomery, M.T., Smith, R.K. and McWilliams, J. (2019) On the realism of quasi-steady hurricanes. *Tropical Cyclone Research and Review*, 8, 1–17.

Reasor, P.D., Eastin, M.D. and Gamache, J.F. (2009) Rapidly intensifying hurricane *Guillermo* (1997). Part I: low-wavenumber structure and evolution. *Monthly Weather Review*, 137, 603–631.

Rogers, R.F., Reasor, P.D. and Lorsolo, S. (2013) Airborne Doppler observations of the inner-core structural differences between intensifying and steady-state tropical cyclones. *Monthly Weather Review*, 141, 2970–2991.

Rotunno, R. and Emanuel, K.A. (1987) An air–sea interaction theory for tropical cyclones. Part II. Evolutionary study using a nonhydrostatic axisymmetric numerical model. *Journal of the Atmospheric Sciences*, 44, 542–561.

Sanger, N.T., Montgomery, M.T., Smith, R.K. and Bell, M.M. (2014) An observational study of tropical-cyclone spin-up in supertyphoon *Jangmi* from 24 to 27 September. *Monthly Weather Review*, 142, 3–28.

Shapiro, L.J. and Willoughby, H. (1982) The response of balanced hurricanes to local sources of heat and momentum. *Journal of the Atmospheric Sciences*, 39, 378–394.

Shin, S. and Smith, R.K. (2008) Tropical-cyclone intensification and predictability in a minimal three-dimensional model. *Quarterly Journal of the Royal Meteorological Society*, 134, 1661–1671.

Smith, R.K. (2006) Accurate determination of a balanced axisymmetric vortex. *Tellus A*, 58, 98–103.

Smith, R.K. and Montgomery, M.T. (2015) Towards clarity on understanding tropical cyclone intensification. *Journal of the Atmospheric Sciences*, 72, 3020–3031.

Smith, R.K. and Montgomery, M.T. (2016) Understanding hurricanes. *Weather*, 71, 219–223.

Smith, R.K., Montgomery, M.T. and Persing, J. (2014) On steady-state tropical cyclones. *Quarterly Journal of the Royal Meteorological Society*, 140, 2638–2649.

Smith, R.K. and Wang, S. (2018) Axisymmetric balance dynamics of tropical cyclone intensification: diabatic heating versus surface friction. *Quarterly Journal of the Royal Meteorological Society*, 144, 2350–2357.

Smith, R.K., Zhang, J. and Montgomery, M.T. (2016) The dynamics of intensification in an HWRF simulation of hurricane *Earl* (2010). *Quarterly Journal of the Royal Meteorological Society*, 143, 293–308.

Stern, D.P., Kepert, J.D., Bryan, G. and Doyle, J.D. (2020) Understanding atypical mid-level wind speed maxima in hurricane eyewalls. *Journal of the Atmospheric Sciences*, 77, 1531–1557.

Wang, S. and Smith, R.K. (2021) Upper-level trajectories in the prototype problem for tropical cyclone intensification. *Quarterly Journal of the Royal Meteorological Society*, 147. https://doi.org/10.1002/qj.4110

Wang, S., Smith, R.K. and Montgomery, M.T. (2020) Upper-tropospheric inflow layers in tropical cyclones. *Quarterly Journal of the Royal Meteorological Society*, 146, 3466–3487.

Wang, Y. (2002) An explicit simulation of tropical cyclones with a triply nested movable mesh primitive equation model: TCM3. Part II: model refinements and sensitivity to cloud microphysics parameterization. *Monthly Weather Review*, 130, 3022–3036.

Willoughby, H.E. (1979) Forced secondary circulations in hurricanes. *Journal of Geophysical Research*, 84, 3173–3183.

Willoughby, H.R., Marks, F.D. and Feinberg, R.J. (1984) Stationary and propagating convective bands in hurricanes. *Journal of the Atmospheric Sciences*, 41, 3189–3211.

Wirth, V. and Dunkerton, T.J. (2006) A unified perspective on the dynamics of axisymmetric hurricanes and monsoons. *Journal of the Atmospheric Sciences*, 63, 2529–2547.

Zhang, J.A. and Montgomery, M.T. (2012) Observational estimates of the horizontal eddy diffusivity and mixing length in the low-level region of intense hurricanes. *Journal of the Atmospheric Sciences*, 69, 1306–1316.

Zhang, J.A., Rogers, R.F., Nolan, D.S. and Marks, F.D. (2011) On the characteristic height scales of the hurricane boundary layer. *Monthly Weather Review*, 139, 2523–2535.

How to cite this article: Smith, R.K., Kilroy, G. & Montgomery, M.T. (2021) Tropical cyclone life cycle in a three-dimensional numerical simulation. *Quarterly Journal of the Royal Meteorological Society*, 147(739), 3373–3393. Available from: https://doi.org/10.1002/qj.4133

APPENDIX. CHOICE OF NEWTONIAN COOLING TIME-SCALE

A challenge that must be confronted in formulating any long-term integration of a tropical cyclone model is how to represent the physical processes (radiation and convection) that determine in part the thermodynamic profiles in the environment. If one models radiation directly in a simulation, the environment profiles must evolve with time until some quasi-radiative-convective equilibrium is achieved in the outer part of the domain. Since a realistic simulation of radiative-convective equilibrium in the Tropics would require a domain size of $5{,}000 \times 5{,}000\,\mathrm{km}^2$ that is at least as large or even larger than a typical domain size used to simulate the cyclone (i.e., many thousands of km), such an approach is not feasible (e.g., Jakob *et al.*, 2019).

For the above reason, it has become traditional to apply Newtonian relaxation to the temperature (or equivalently potential temperature) field, relaxing the temperature in and around the storm to that of the environment on a prescribed time-scale (e.g., Rotunno and Emanuel, 1987 and many others). This procedure, while certainly crude, is simply an expedient to obtain a closed formulation that does not allow an appreciable warming of the storm environment in the upper troposphere. In reality, such cooling would be accomplished by infrared radiation to space.

With the relaxation formulation, the next question is what relaxation time-scale to choose? Rotunno and Emanuel chose 12 hr on the basis that this value "yields cooling rates of approximately $2\,\mathrm{K{\cdot}day^{-1}}$ in the outer regions and is approximately enough to balance the gentle, but persistent subsidence in the outer regions of the vortex". However, they noted that this choice "produces unrealistically large cooling rates in the inner core", which has undesirable consequences for the parcel buoyancies produced in the eyewall (their section 3e). For these reasons they carried out tests in which the magnitude of local cooling was not allowed to exceed $2\,\mathrm{K{\cdot}day^{-1}}$ and one in which cooling was dispensed with altogether. They found, *inter alia*, that the simulation without Newtonian cooling "produces a colder outflow (and a more intense vortex)".

As part of their study of dry layers that are frequently observed in atmospheric soundings from the climatologically humid western Pacific warm pool region, Mapes and Zuidema (1996) examined the effects of radiation on thermal and moisture perturbations typical of those generated through gravity waves produced in the environment of tropical mesoscale convective systems. These waves lead to downward displacements (causing positive temperature and negative humidity anomalies) in the upper troposphere above the 500 mb level and upward displacements (causing negative temperature and positive humidity anomalies) below (Mapes, 1993; Mapes and Houze, 1995).

Mapes and Zuidema applied such a vertical displacement profile to the mean tropical sounding from their study and computed clear-air radiative cooling rates using the resulting profiles for two cases: one in which the displacement affected the temperature only and one in which the displacement acted upon both the temperature and humidity fields. They showed that the radiative cooling rates calculated from the temperature perturbation alone were close to those based on a Newtonian cooling formulation with a relaxation time-scale of 10 days rather than 12 hr. However, they pointed out that humidity variations are somewhat more important in their radiative cooling calculations than just the temperature variations alone. These results serve to reinforce the acknowledged crudity of the physics embodied in the Newtonian relaxation procedure, which does not consider the moisture field.

In the absence of obvious viable alternatives to employing Newtonian relaxation in the present study, we performed three idealized 16-day hurricane simulations that included an RI phase, a short (∼ 3 day) first mature phase, a brief period of decay and reintensification, a longer second mature phase and a decay phase (not shown). One experiment kept the default 12 hr time-scale in CM1 for relaxation (following Rotunno and Emanuel, 1987), another used the 10 day time-scale suggested by Mapes and Zuidema (1996), p. 631, while the third simulation contained no relaxation to the background state. In the simulation with the 10 day time-scale, there is a progressive warming of the entire domain. At mid to upper levels, the warming is greater than 4 K over 16 days and the system-scale vortex decays markedly during this time. The vortex in the simulation with no relaxation evolved in a similar way to that with the 10 day time-scale, although in that case the warming was about 1 K larger. With a 12 hr time-scale, the temperature of the outer domain remains very close to the initial sounding and the vortex takes much longer to decay. Like the finding of Rotunno and Emanuel (1987), the simulation without cooling produces a slightly more intense vortex (not shown).

The mid- and upper-level warming of the environment that occurs with the 10-day relaxation time-scale is not necessarily unrealistic. In fact, in nature there is often a warming of the environment surrounding tropical cyclones. In a study of real-world events in the ECMWF operational analyses, the large-scale environment surrounding tropical cyclones in the upper troposphere warms on the order of about 2–4 K. This warming is illustrated in Figure A1, which shows the time–height cross-sections of the areally averaged temperature difference on an isobaric surface in a 10° × 10° column following two tropical cyclones *Georges* and *Carlos*, which occurred in the Australian region[5] (Kilroy *et al.*, 2017a). These observationally constrained analyses, which include sophisticated representations of radiation (Hogan and Bozzo, 2018), suggest that the default time-scale for relaxation in CM1 is strongly over-relaxing to the initial sounding in the case of a mature tropical cyclone.

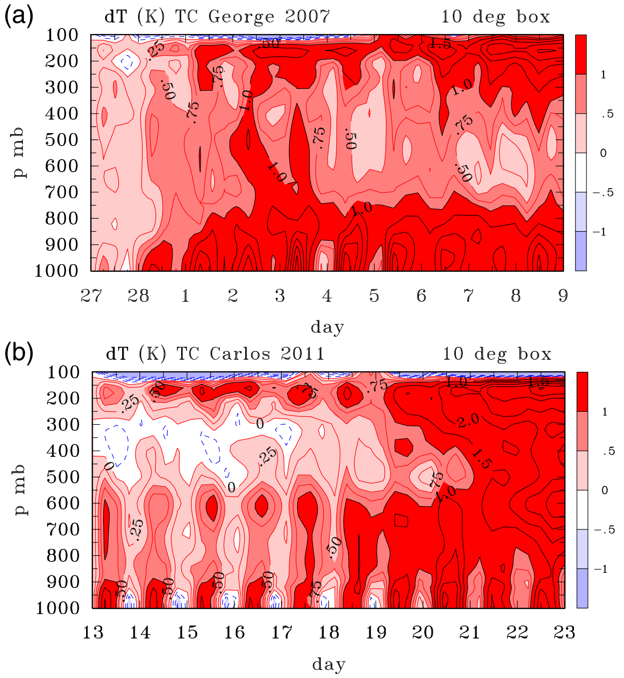

FIGURE A1 Time–height cross section of areally averaged temperature deviation (shading, K) from that at the start of the time series within a column 10° × 10°, centred on the location of the minimum geopotential at 850 mb for the development of tropical cyclones (a) *Georges* (27 January–9 February 2007) and (b) *Carlos* (13–23 February 2011). Additional contours every 0.5 K. This figure was constructed from the ECMWF operational analysis, which has a horizontal grid spacing of 0.125 deg and a temporal output of 6 hr. The evolution of TC *Georges* is described in more detail in Kilroy *et al.* (2017) [Colour figure can be viewed at wileyonlinelibrary.com]

---

[5] In addition to the upper-tropospheric warming, these storms reveal a lower-tropospheric warming with a prominent diurnal cycle associated with the land track of these systems.